

UNIVERSITY OF CALIFORNIA,
IRVINE

An Advanced Deep Learning and Computer Vision Framework for Precipitation Retrieval
from Multi-spectral Satellite Information

submitted in partial satisfaction of the requirements
for the degree of

DOCTOR OF PHILOSOPHY
in Civil and Environmental Engineering

by

Negin Hayatbini

Committee:
Professor Soroosh Sorooshian, Chair
Professor Kuo-lin Hsu
Professor Amir Aghakouchak

2020

© 2020 Negin Hayatbini

DEDICATION

To my beloved parents;

The pure source of joy, love, and passion.

TABLE OF CONTENTS

	Page
LIST OF FIGURES	v
LIST OF TABLES	vii
ACKNOWLEDGMENTS	viii
CURRICULUM VITAE	x
ABSTRACT OF THE	xiii
1 Introduction	1
1.1 Precipitation Retrieval from Satellite Information	1
1.2 Research Motivation and Objectives	3
2 Background	7
2.1 Overview of Satellite-Based Precipitation Estimation and the Challenges . . .	7
2.1.1 Threshold as a Controlling Factor in Cloud Segmentation	9
2.1.2 Imbalance of Precipitation Data	9
2.1.3 Infusion of Multiple Sources of Remotely Sensed Information as Input	10
2.2 Computer Vision Applications on Satellite Imageries	10
2.3 Overview of Deep Neural Networks	11
3 Cloud Detection and Segmentation from Multi-spectral Satellite Information	14
3.1 Introduction	14
3.2 Methodology	15
3.2.1 GMS Framework for Cloud Detection and Segmentation	15
3.3 Description of the Dataset	21
3.3.1 GOES-16 ABI	21
3.3.2 PSU WRF-EnKF Dataset	22
3.4 Results and Discussion	23
3.4.1 Visual Comparison	23
3.4.2 Statistical Evaluation	28
3.5 Summary and Conclusions	31

4 Rain/Norain Detection and Rainfall Estimation from Multispectral Satellite Information	33
4.1 Introduction	33
4.2 Materials and Study Region	34
4.3 Methodology and Model Setup	35
4.4 Results and Discussion	44
4.5 Conclusion	49
5 Summary and Conclusion	52
5.1 Dissertation Summary and conclusion	52
5.2 Future Directions	54
5.2.1 Additional Data Sources	54
5.2.2 Model Development	55
5.2.3 Operational Application	56
Bibliography	57

LIST OF FIGURES

	Page
2.1 PERSIANN-CCS algorithm structure.	8
3.1 Flow diagram of the proposed multi-spectral gradient-based segmentation algorithm.	16
3.2 Histogram plot of the gradient magnitude image. Horizontal axis is showing the range of gradient magnitude values, and the vertical axis is the number of pixels with each gradient magnitude value.	19
3.3 Watershed Transformation Process Diagram. Each of the positive signs represents one watershed domain.	20
3.4 Effect of increasing the threshold on the Watershed segmentation technique. The positive (negative) signs are representing the seeds that are included (excluded) in the segmentation process.	21
3.5 Visualization of the gradient based segmentation result for simulated Hurricane Harvey event on August 26th 2017 at 3:00 AM UTC.	24
3.6 Visualization of the gradient based segmentation result for the simulated Wyoming tornado event at 21:20 UTC of the 12th of June 2017.	24
3.7 Visual comparison of the two segmentation output (B and C) based on the 'truth' mask as a reference for the simulated Hurricane Harvey event at 3:00 AM UTC of August 26th 2017.	25
3.8 Visual comparison of the two segmentation output (B and C) based on the 'truth' mask as a reference for the the simulated Wyoming tornado event at 21:20 UTC of the 12th of June 2017.	26
3.9 Visualizing the effect of integrating complementary information from lower-level water vapor for the Wyoming tornado case at 21:05 UTC of the 12th of June 2017.	27
3.10 Statistical comparison of two different segmentation algorithms for Hurricane Harvey case.	30
3.11 Statistical comparison of two different segmentation algorithms for Wyoming Tornado case.	31
4.1 The proposed framework for the Precipitation Estimation.	36
4.2 Visualized structure of U-net network.	38
4.3 Schematic conditional Generative Adversarial Network Structure.	42

4.4	a) Channels 10 and b) 13 from ABI GOES-16 imagery, c) cGAN model half hourly output, d) PERSIANN-CCS half hourly precipitation values, and e) The MRMS data for July 31, 2018 at 22:00 UTC over the CONUS. Black circles on GOES-16 satellite imageries are presenting regions with warm clouds and the red circles are the corresponding regions with the rainfall associated with the warm clouds.	46
4.5	Daily (left panel) and monthly (right panel) precipitation values for a&d) PERSIANN-CCS, c&f) cGAN model output compared to the b&e) Reference data - MRMS. Red circles are highlighting regions with most of the differences.	47
4.6	Visualization of precipitation identification performance of PERSIANN-CCS vs cGAN model output over the United States for July 20th, 2018.	48
4.7	POD (top row), FAR (middle row), and CSI (bottom row) of PERSIANN-CCS (left column), the baseline model (middle column), and the cGAN model (right column) over the United States for July 2018.	49
4.8	The Correlation and MSE values ($mm\ h^{-1}$) ² for the cGAN and PERSIANN-CCS model over the CONUS and during the validation period (month of July 2018).	50

LIST OF TABLES

	Page
3.1 The four possible diagnosis results of testing.	28
3.2 Verification Metrics	29
4.1 Parameters for channel normalization applied using the formula: $\frac{value - min}{max - min}$	37
4.2 Details of network architectures.	39
4.3 Description of the verification metrics.	39
4.4 Common verification measures for the satellite-based precipitation estimation products.	40
4.5 Statistical evaluation metrics values for different scenarios using single spectral bands	44
4.6 Statistical evaluation metrics values for different scenarios using multiple spectral bands	45

ACKNOWLEDGMENTS

Alongside the scientific contributions of my graduate study, my time at UCI has been endowed with more personal and professional growth than I could have ever imagined. I would like to express my gratitude to the many people who had roles in creating such an exceptional experience that I will forever cherish. Just a few sentences do not do justice to the impact they have had on me, but I hope to pay forward what I've thought.

I cannot thank my advisor distinguished Professor Soroosh Sorooshian enough for his tremendous support and inspiration throughout the years. I feel blessed and grateful to have him and his wife, Shirin Sorooshian in my life who always made me feel like a part of the family from the very beginning of stepping into the UCI. Professor Sorooshian, I am greatly indebted to you for all the wisdom, joy, and compassion you shared with me. I would also like to sincerely thank my co-advisor, Professor Kuolin Hsu for his technical supports, helping me to nourish my ideas until they are completely developed. Professor Hsu, thank you very much for all your scholarly and professional guidance. I would also like to thank my Ph.D. committee member, Professor Amir Aghakouchak for his unconditional support and enlightening comments and thoughts he shared with me during my studies. I want to also thank CHRS colleagues including Dr. Phu Nguyen, Dr. Bita Analui, Diane Hohnbaum, and Dan Braithwaite for their efforts supporting students at CHRS. I would also like to deeply thank all my friends at UCI, and all over the United States, who have always been there for me as a family.

I am thankful to Prof. Charless Fowlkes, one of my candidacy exam committee members and his student Dr. Baily Kong from the computer science department. They have been always very welcoming to support and give technical advice on my dissertation. Working closely with Dr. Kong helped me widening my vision in the field of Deep Learning and Computer Vision which builds the main blocks of my dissertation. I would also like to thank late Prof. Fuqing Zhang who kindly invited me to spend time and collaborate with his amazing group at the Penn State Center for Advanced Data Assimilation and Predictability Techniques (PSU-ADAPT). He was a great scientist and his death was a big loss for the science community. May he rest in peace and his legacy be cherished forever. I would like to cordially thank Dr. Graeme Stephens for his attention to my work. I am honored and grateful to be the recipient of the NASA JPL award for my research proposal and I am grateful that he always takes the time listening to my research ideas and giving professional guidance. I would also like to thank scientists at NASA Ames/ Bay Area Environmental Research Institute (BAERI) which I spent time with them for a while as an intern - research scientist and was inspired by the cutting edge research projects they are conveying. I enjoyed my time collaborating and sharing my research outcome with Dr. Ramakrishna Nemani and am grateful for that.

My greatest appreciation goes to my beloved parents, Dr. Majid Hayatbini, and Zarin Rezaei-Azar who although I couldn't have them by my side during the past five years, this journey wouldn't be possible without their constant love, support, and inspiration. They are the reason for who I am and where I am standing in life and are the role model of mine in

dedication, kindness, love, diligence, and passion. I hope this could be considered as a small appropriation for at least part of their sacrifices and makes them happy and proud. I am also blessed for having the most loving, supporting and encouraging siblings, Niki and Ali who I find myself the happiest whenever I even think of them.

The financial supports of this research are from U.S. Department of Energy (DOE Prime Award No. DE-IA0000018), California Energy Commission (CEC Award No. 300-15-005), MASEEH fellowship, NASA MIRO grant (NNX15AQ06A), and NASA—Jet Propulsion Laboratory (JPL) Grant (Award No. 1619578).

CURRICULUM VITAE

Negin Hayatbini

EDUCATION

Doctor of Philosophy in Civil and Environmental Engineering University of California, Irvine	2020 <i>Irvine, CA</i>
Master of Science in Civil Engineering Sharif university of Technology	2014 <i>Tehran, Iran</i>
Bachelor of Science in Civil Engineering University of Zanjan	2011 <i>Zanjan, Iran</i>

AWARDS AND HONORS

Student Research Proposal Award (Grant Award #1619578) NASA JPL	January 2019 <i>Pasadena, CA</i>
Outstanding Engineering Student Award Orange County Engineering Council (OCEC)	February 2018 <i>Orange County, CA</i>
Best Graduate Student Presentation Award Graduate Research Symposium, University of California, Irvine	April 2018 <i>Irvine, CA</i>
Selected California Science Translator California Council on Science and Technology (CCST)	December 2018 <i>California State Capitol, CA</i>
NSF Summer Public Policy Colloquium Award AMS (American Meteorological Society)	June 2017 <i>Washington, D.C.</i>
Department of Energy CERC-WET Funding Fellowship University of California, Irvine	June 2016 <i>Irvine, CA</i>
MASEEH Fellowship University of California, Irvine	September 2016 <i>Irvine, CA</i>

TECHNICAL SUMMER SCHOOLS

Using Satellite Observations to Advance Climate Models NASA's Earth Science Division -JPL Center for Climate Sciences (CCS)	Summer 2017 <i>Pasadena, CA</i>
Network for Sustainable Climate Risk Management (SCRiM) Pennsylvania State University	Summer 2018 <i>Pennsylvania, PA</i>

RESEARCH EXPERIENCE

Graduate Research Assistant Center for Hydrometeorology and Remote Sensing (CHRS)	2015–2020 <i>Irvine, CA</i>
Part-time Research Scientist - Intern NASA Ames / Bay Area Environmental Research Institute (BAERI)	Summer 2019 <i>Moffett Field, CA</i>
Scholarized Visiting Researcher at Penn State University Center for Advanced Data Assimilation and Predictability Techniques	Fall 2018 <i>Pennsylvania, PA</i>

TEACHING EXPERIENCE

Engineering Hydrology - Voluntary University of California, Irvine	Fall 2017 & 2019 <i>Irvine, CA</i>
Advanced Predictive Modeling with Python University of California, Irvine Data Science Initiative	Fall 2018 <i>Irvine, CA</i>
Application of GIS and RS in Water Resources Management Sharif University of Technology	Fall 2013 <i>Tehran, Iran</i>

EDITORIAL AND REVIEWER SERVICES

Review Board Member Remote Sensing Journal	Since October 2019
Awarded Reviewer Certificate International Journal of Climatology	July 2019

REFEREED JOURNAL PUBLICATIONS

Hayatbini, N., Kong, B., Hsu, K.L., Nguyen, P., Sorooshian, S., Stephens, G., Fowlkes, C., Nemani, R. and Ganguly, S., 2019. Conditional Generative Adversarial Networks (cGANs) for Near Real-Time Precipitation Estimation from Multispectral GOES-16 Satellite Imageries — PERSIANN-cGAN.
Remote Sensing 11 (19), 2193.

Hayatbini, N., Hsu, K.L., Sorooshian, S., Zhang, Y. and Zhang, F., 2019. Effective Cloud Detection and Segmentation Using a Gradient-Based Algorithm for Satellite Imagery: Application to Improve PERSIANN-CCS.
Journal of Hydrometeorology, 20(5), pp.901-913.

Nguyen, P., Shearer, E.J., Tran, H., Ombadi, M., **Hayatbini, N.**, Palacios, T., Huynh, P., Braithwaite, D., Updegraff, G., Hsu, K. and Kuligowski, B., 2019. The CHRS Data Portal, an easily accessible public repository for PERSIANN global satellite precipitation data.

Nature: Scientific Data 6 (2019): 180296.

Yang, T., Asanjan, A.A., Faridzad, M., **Hayatbini, N.**, Gao, X. and Sorooshian, S., 2017. An enhanced artificial neural network with a shuffled complex evolutionary global optimization with principal component analysis. Information Sciences 418 (2017): 302-316.

ORAL AND POSTER PRESENTATIONS

Hayatbini, N., Kong, B., Hsu, K.L., Nguyen, P., Sorooshian, S. and Stephens, G.L., 2019, December. A Deep Learning Framework for Precipitation Estimation from GOES-16 multispectral satellite imagery-Application of the conditional Generative Adversarial Networks (cGANs). In AGU Fall Meeting Abstracts.

Hayatbini, N., Hsu, K.L., Sorooshian, S. and Nguyen, P., 2018, December. An Effective Gradient-Based Cloud Segmentation and Detection Algorithm for Multi-Spectral Satellite Imagery. In AGU Fall Meeting Abstracts.

Hayatbini, N., Hsu, K.L., Yang, T. and Sorooshian, S., 2017, December. Developing a Storm Tracking Algorithm using Satellite Image Segmentation and Optical Flow Techniques. In AGU Fall Meeting Abstracts.

Hayatbini, N., Faridzad, M., Yang, T., Akbari Asanjan, A., Gao, X. and Sorooshian, S., 2016, December. A New Artificial Neural Network Enhanced by the Shuffled Complex Evolution Optimization with Principal Component Analysis (SP-UCI) for Water Resources Management. In AGU Fall Meeting Abstracts.

SOFTWARE

Programming: Professional in Python, familiar with MATLAB and R

Operating Systems: Linux, High Performance Clusters (HPC), Kubernetes

CERTIFICATES

Data Science Program Certificate of Completion. December 2018
University of California, Irvine Data Science Initiative

AMS Summer Policy Colloquium. June 2017
American Meteorological Society

Excellence in Engineering Communications. March 2018
The Graduate Division at the University of California, Irvine

ABSTRACT OF THE DISSERTATION

An Advanced Deep Learning and Computer Vision Framework for Precipitation Retrieval
from Multi-spectral Satellite Information

By

Negin Hayatbini

Doctor of Philosophy in Civil and Environmental Engineering

University of California, Irvine, 2020

Professor Soroosh Sorooshian, Chair

Among all natural phenomena, precipitation is the main driver of the hydrological cycle and the challenging task of precipitation estimation is an essential element for hydrological and meteorological applications. Recent developments in satellite technologies resulting in higher temporal, spatial, and spectral resolutions, along with advancements in Machine Learning (ML) algorithms and computational power, open the great opportunity to develop analytical and data-driven tools to characterize such natural phenomena and their future behavior more efficiently and accurately. In this dissertation, state-of-the-art data-driven frameworks are proposed based on advanced deep learning algorithms and computer vision tools to extract the most useful features from single or multiple spectral bands of satellite information.

Specifically, in the first part of the dissertation, a novel gradient-based cloud segmentation algorithm is proposed to effectively identify clouds and monitor their evolution towards more accurate quantitative precipitation estimation and forecast. This algorithm integrates morphological image gradient magnitudes to separate cloud systems and patches boundaries from single or multi-spectral imagery. This method improves rain detection and estimation skills with an accuracy rate of up to 98% in identifying cloud regions compared to the existing cloud-patch-based segmentation technique implemented in the operational PERSIANN-CCS

(Precipitation Estimation from Remotely Sensed Information using Artificial Neural Network - Cloud Classification System) algorithm. Application of this method is extendable to hurricanes simulations and synthetic satellite imageries simulated by high-resolution weather prediction models.

In the second part, an end-to-end deep learning precipitation estimation framework is developed from multiple sources of remotely sensed information to provide half-hourly, 4-km by 4-km precipitation estimates over the CONUS. In the first stage, a Rain/No Rain (R/NR) binary mask is generated by classification of the pixels and then a Fully Convolutional Network (FCN), U-net, is used as a regressor to predict precipitation estimates for rainy pixels. Due to the complex structure of precipitation, and inability of traditional objective functions to capture the true rainfall distribution, a novel distribution matching approach is designed and implemented. The network is trained using both the conditional Generative Adversarial Network (cGAN), and the Mean Squared Error (MSE) loss terms to match the distribution of the generated results and observed data, and to relax the strict assumptions of the traditional and conventional loss function in DNNs. The newly developed precipitation estimation algorithm is introduced as an augmentation for PERSIANN-CCS (Precipitation Estimation from Remotely Sensed Information using Artificial Neural Network - Cloud Classification System) algorithm for estimating global precipitation and is termed as PERSIANN-cGAN. Statistics and visualizations of the metrics for PERSIANN-cGAN represent an improvement of the precipitation retrieval accuracy compared to the operational PERSIANN-CCS product, and a baseline model trained using the conventional MSE loss term.

Chapter 1

Introduction

1.1 Precipitation Retrieval from Satellite Information

Effective water resources engineering and management is a necessity for the growing global demand for water, energy and food security nexus. Therefore, continuous and accurate measurement of precipitation on a global scale has become a top priority. There are several precipitation measurement techniques, each with its own advantages and disadvantages. Rain gauges are the traditional ground-based measures that are associated with drawbacks such as calibration errors. They also fail to provide measures for remote areas with poor accessibility. Ground-based radars are another source of information for precipitation measurement and are available in higher temporal and spatial resolutions. However, they have disadvantages such as beam blockage, attenuation, and calibration. Such limitations make the remotely sensed information an ideal candidate for precipitation estimation tasks with higher spatial and temporal resolution and with global coverage. Geostationary Earth Orbit (GEO) and Low Earth Orbit (LEO) satellite instruments are the most commonly used sources of information for precipitation retrieval. The Passive microwave (PMW) information

from sensors onboard Low-Earth-Orbiting (LEO) satellites is more relevant to the vertical hydrometeor distribution and surface rainfall, due to the response of microwave frequencies to ice particles or droplets associated with precipitation. Although PMW observations from LEO satellites have broader spatial and spectral resolutions, less frequent sensing can result in uncertainty for the spatial and temporal accumulation of rainfall estimation (Joyce et al., 2004; Kidd et al., 2003; Marzano et al., 2004).

IR from GEO satellites is considered as unique means to provide cloud-rain information continuously over space and time due to their placement into an orbit that rotates the same direction as the earth does. GEO satellites sensors provide both visible (VIS) and long-wave infrared (IR) relevant to cloud top temperature and albedo. Utilization of both GEO and LEO satellites information in precipitation retrieval algorithms proven to be a strength for this task. An example of using LEO-PMW satellite data along with the GEO-IR-based data to provide global precipitation estimation at near real-time is the Global Precipitation Measurement (GPM) mission. The NASA GPM program provides a key dataset called Integrated Multi-satellite Retrievals for GPM (IMERG). IMERG has been developed to provide half-hourly global precipitation monitoring at $0.1^\circ \times 0.1^\circ$ (Huffman et al., 2015). The satellite-based estimation of IMERG consists of three groups of algorithms including the Climate Prediction Center (CPC) morphing technique (CMORPH) from NOAA Climate Prediction Center (CPC) (Joyce et al., 2004), the Tropical Rainfall Measuring Mission (TRMM) Multi-satellite Precipitation Analysis from NASA Goddard Flight Center (TMPA) (Huffman et al., 2007), and microwave-calibrated Precipitation Estimation from Remotely Sensed Information using Artificial Neural Networks - Cloud Classification System (PERSIANN-CCS) (Hong et al., 2004). PERSIANN-CCS is a data-driven algorithm that uses exponential regression to estimate the precipitation from cloud patches at 0.04° by 0.04° spatial resolution based on an unsupervised neural network (Hong et al., 2004).

Application of Deep Neural Networks in science and weather/climate studies is expanding

and has been implemented in many studies including but not limited to short term precipitation forecast (Akbari Asanjan et al., 2018), statistical downscaling for climate models (Vandal et al., 2017), extreme weather detection (Liu et al., 2016), and precipitation estimation (Tao et al., 2016, 2017). Significant advances of DNNs include Convolutional Neural Networks (CNNs) (LeCun et al., 1989), Recurrent Neural Networks (RNNs) (Elman, 1990; Jordan, 1997), and generative models. Variational AutoEncoder (VAE) (Vincent et al., 2008; Pu et al., 2016) and Generative Adversarial Network (GAN) (Goodfellow et al., 2014) are among the popular types of generative models. Each of the networks has strength in dealing with different types of datasets. CNNs benefit from convolution transformation to deal with spatially and temporally coherent datasets (LeCun et al., 1989; Krizhevsky et al., 2012). RNNs can effectively process information in the form of time-series and learn from a range of temporal dependencies in datasets. Generative models are capable of producing detailed results from limited information and provide a better match to observation data distribution by updating conventional loss function in DNNs.

1.2 Research Motivation and Objectives

The general motivation for this dissertation is to address the global need for a better understanding and management of water resources, which is particularly urgent as climate change has begun to significantly alter climate patterns. Simultaneously, the world's growing population requires increasing access to freshwater for drinking and sanitation. This task requires precise, adaptive modeling of climate systems, as rainfall and other forms of precipitation play an integral role in the worldwide water cycle. PERSIANN-CCS is among global operational precipitation retrieval algorithms that are currently in use, to produce rainfall estimates. The processing steps of PERSIANN-CCS algorithm include (1) cloud image segmentation, (2) image feature extraction and classification, and (3) rainfall

mapping. Although PERSIANN-CCS has high spatial and temporal resolutions, it may sometimes overestimate or underestimate rainfall amount due to some of its inherent limitations (Behrangi et al., 2009a). Despite recent developments to advance PERSIANN-CCS (Karbalaee et al., 2017; Tao et al., 2016; Nasrollahi et al., 2013; Mahrooghy et al., 2012; Behrangi et al., 2009a), little attention is paid to improve the uncertainties associated with its cloud segmentation algorithm. Cloud image segmentation is the first and one of the most important steps in all precipitation retrieval algorithms.

The threshold-based segmentation methods are the most broadly applied techniques in cloud detection for satellite-based precipitation retrieval algorithms because they are simple, fast and have agreeable accuracy (Hagolle et al., 2010; Jedlovec et al., 2008; Zhu et al., 2015). In threshold-based techniques, clouds are generally differentiated by a higher reflectance or lower temperature than the background or earth surface. A major source of error for this type of approach comes from the complex land surface composition and the high variability of reflectivity in different cloud types. A threshold that is appropriate to a certain cloud type or a certain geographical region may not be applicable for another (Sun et al., 2016). Moreover, pixels defined by the threshold can only consider the radiometric and textural features of an individual pixel rather than contextual information provided by the image regions as objects (Blaschke et al., 2014). Hence, the implementation of an object-based approach designed to segment the clouds into meaningful objects independent of the predetermined threshold is superior to the threshold-based segmentation techniques in the context of patch-based precipitation retrieval algorithms.

In addition to the disadvantages of threshold-based algorithms, the IR-based rainfall estimation algorithms including PERSIANN-CCS rely on the assumption that colder cloud-top brightness temperature indicates higher precipitation probability (Kidd et al., 2003; Huffman et al., 2007; Levizzani et al., 2001). However, different types of clouds may have similar cloud-top brightness temperatures in longwave IR channels (Sorooshian et al., 2000). Mea-

surements from different channels can provide additional information about the structure and vertical profile of clouds that lead to more accurate rain estimates (Xu et al., 2005).

Effective use of the available big data from multiple bands and sensors is of great importance to improve the accuracy of precipitation estimation products (Tao et al., 2018). Recent developments of Machine Learning (ML) techniques have been extended to the geosciences community and is another motivation to improve the accuracy of satellite-based precipitation estimation products (Bengio, others, 2009; Hinton, 2009; LeCun et al., 2015; Liu et al., 2015; Tao et al., 2018; Rasp et al., 2018; Reichstein et al., 2019; Akbari Asanjan et al., 2018; Hayatbini et al., 2019a; Pan et al., 2019). Deep Neural Networks (DNNs) are a specific type of ML with great capability to handle a huge amount of data. DNNs are able to train a multiple-stage neural network end-to-end, from raw input data to desired output and proven to be capable of capturing sophisticated distribution of rainfall. This is an important superiority of DNNs over simpler models to better extract and utilize the spatial and temporal structures from huge amounts of geophysical data available from a wide variety of sensors and satellites (Schmidhuber, 2015; Shen et al., 2017).

Specifically, this dissertation addresses the following objectives:

- Demonstrate application of computer vision techniques in cloud segmentation and identification task.
- Provide a framework to capture warm clouds with higher brightness temperature and lower heights that PERSIANN-CCS is not currently capable of capturing them.
- Infusion of multiple spectral bands as well as different sources of information as inputs to the cloud segmentation and detection part of PERSIANN-CCS algorithm in order to improve the accuracy of precipitation estimation.
- Demonstrate the effectiveness of deep learning algorithms for extraction of precipitation

relevant information from multiple sources of information as input and comparing its performance with operational products.

- Design a DL framework that provides a more sophisticated objective function capable of capturing complex rainfall distributions.

The remainder of this dissertation is organized into 4 chapters. Chapter 2 summarizes related background information on precipitation estimation and deep learning techniques. Chapters 3 and 4 describe the main novel contributions of this dissertation. Finally, summary, conclusions and future directions are discussed in Chapter 5.

Chapter 2

Background

2.1 Overview of Satellite-Based Precipitation Estimation and the Challenges

NASA Integrated Multi-satellite Retrieval is a key detest from Global Precipitation Mission (GPM) that provides half-hourly global precipitation monitoring at $0.1^\circ \times 0.1^\circ$. This algorithm - IMERG (Integrated Multi-satellitE Retrievals for GPM) - consists of three algorithms including CMORPH, TRMM, PERSIANN-CCS (Huffman et al., 2015). CMORPH (the Climate Prediction Center (CPC) morphing technique) from NOAA Climate Prediction Center (CPC) (Joyce et al., 2004) tracks the precipitation motion patterns from IR imagery and interpolates between microwave scans. TRMM (the Tropical Rainfall Measuring Mission) is the Multi-satellite Precipitation Analysis from NASA Goddard Flight Center (TMPA) and has different versions (i.e. AMSR-E, TMI, and SSM/I) (Huffman et al., 2007). Microwave-calibrated Precipitation Estimation from Remotely Sensed Information using Artificial Neural Network-Cloud Classification System (PERSIANN-CCS) (Hong et al., 2004) that is used as a baseline model throughout the dissertation.

PERSIANN-CCS uses a cloud-patch based technique and applies artificial neural networks to classify clouds. Precipitation is then estimated based on a relationship between precipitation rates and the cloud top temperatures. Figure 2.1 demonstrates the PERSIANN-CCS algorithm structure.

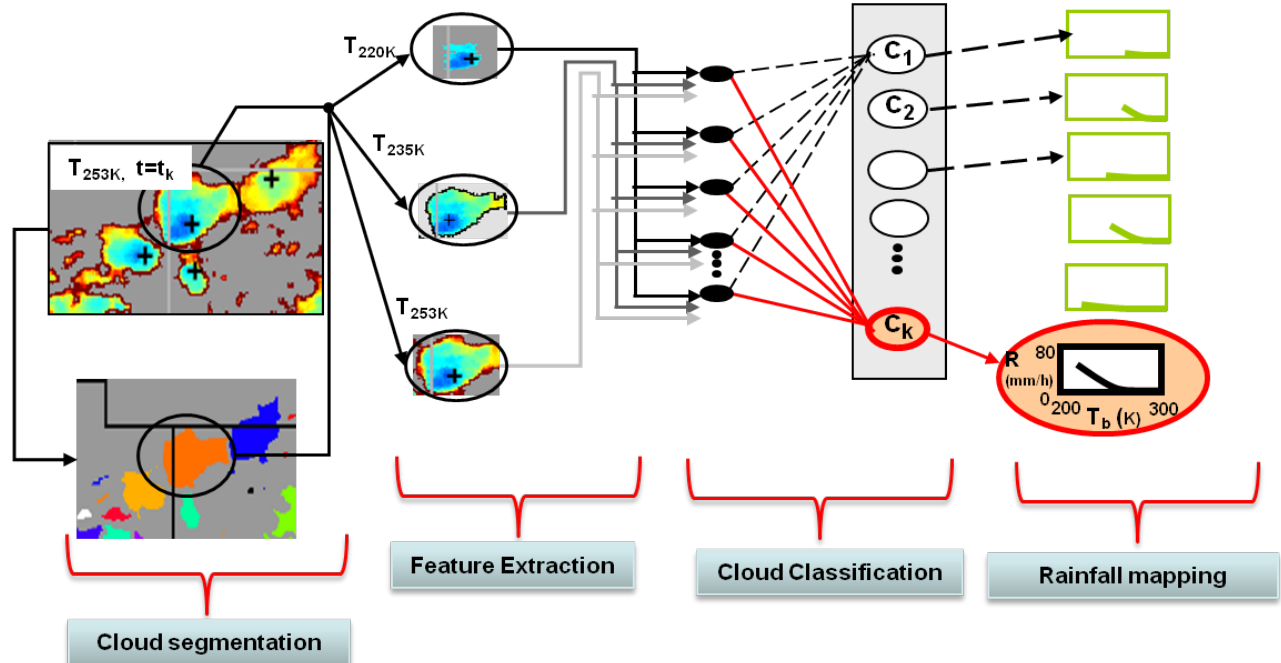


Figure 2.1: PERSIANN-CCS algorithm structure.

PERSIANN-CCS segmentation combines thresholding and Seeded Region Growing (SRG; Adams, Bischof, 1994) algorithm to separate satellite images into distinctive cloud patches (Hong et al., 2004). The minimum brightness temperature ($T_{b\min}$) of the cloud patches are determined to use as seed. Then, the temperature threshold is raised to identify a new set of pixels neighboring the seeded points. This procedure continues until reaching the borders of other seeded regions or cloud-free regions. The temperature threshold is iteratively increased to a maximum of 253 K. Afterward, a morphological operation is applied to merge tiny regions (Hong et al., 2004). Further details of the segmentation process in PERSIANN-CCS precipitation retrieval algorithm can be found in (Hong et al., 2003, 2006).

2.1.1 Threshold as a Controlling Factor in Cloud Segmentation

PERSIANN-CCS algorithm is one of the precipitation retrieval algorithms that estimate rainfall from clouds up to a certain brightness temperature threshold, assuming that no rainfall is associated with clouds with temperature higher than 253k. In other words, pixels with lower brightness temperature at the top of clouds have heavier precipitation on the ground. The reason for this idealized assumption is to ensure that large values can be predicted by the models (Arkin, Meisner, 1987; Hsu et al., 1997). However, such presumption might cause the exclusion of warm clouds that are associated with a considerable amount of rainfall. One main purpose of this dissertation is to introduce the segmentation technique that is independent of threshold and is capable of extracting cloud types regardless of their temperature and height.

2.1.2 Imbalance of Precipitation Data

Precipitation values in high spatiotemporal resolution are highly skewed toward smaller values due to the dominance of no-rain pixels, as well as, the rarity of pixels with heavy rain. This imbalance of precipitation data is a great challenge in applying data-driven methods specifically using simple and common objective measures to serve as the optimization objective for precipitation estimation. This means that using single objective loss functions is insufficient in driving the model to capture the true underlying distribution of precipitation values. In this dissertation, a new objective function consisting of multiple parts is introduced to tackle the challenge of fitting the best distribution for the output from the observation.

2.1.3 Infusion of Multiple Sources of Remotely Sensed Information as Input

Advancement of satellites and sensors on board, has provided an unprecedented opportunity to extract relevant information from multiple sources of space-born information to provide a more comprehensive understanding of natural phenomena. Precipitation estimation using multi-channel information is expected to outperform algorithms that are using single spectral bands. For example, (Behrang et al., 2009b) used Multispectral Analysis to improve rain/no rain detection capabilities. They found that combining any two IR channels in the rain retrieval algorithm seems superior to the one using a single IR channel, and an improvement on the rain rate statistics can be gained.

Many internationally sponsored satellite missions provide valuable information to estimate precipitation including NASA (The National Aeronautics and Space Administration), NOAA (National Oceanic and Atmospheric Administration), and EUMETSAT (European Organization for the Exploitation of Meteorological Satellites). This dissertation proposes frameworks that are capable of infusing multiple types of information as inputs such as multiple spectral bands, sensors, topography maps as well as observations and as a result, provide a more realistic understanding of the problem.

2.2 Computer Vision Applications on Satellite Imagery

In the area of computer vision, Mathematical Morphology (MM) plays an essential role. Mathematical morphology was originally developed at the Paris School of Mines as a set-theoretical approach to image analysis Serra (1983) Matheron (1975). Morphological analysis of an Image includes studying image transformation with simple geometrical interpretation, as well as set operations to images and their operators Roerdink (1996).

The importance and impact of image processing and mathematical morphology are well documented in areas ranging from automated vision detection and inspection to object recognition, image analysis, image augmentation, and pattern recognition. Among the applications in the field of remote sensing Chen et al. (2014), Zhang et al. (2016), Zhu et al. (2017), semantic segmentation to identify and extract clouds is the main focus of this dissertation.

2.3 Overview of Deep Neural Networks

Deep Neural Networks (DNNs) are the latest generation of Artificial Neural Networks (ANNs) Schmidhuber (2015) with more complex mathematical modeling to process data in sophisticated ways Goodfellow et al. (2016). ANNs consist of neurons or units with certain activation and parameters with layers between input and output referred to as "hidden" layers. DNNs are considered as ANNs containing multiple hidden layers Ma et al. (2019). DNNs obtain a representation of the input space by extracting high-level features from a large amount of data using statistical learning. The deep architecture of DNNs results in their performance superiority over human in term of accuracy for some domainsBengio, others (2009). However, this comes with the cost of high-computational complexity which will become manageable by efficient use of graphics processing units (GPU), rectified linear units (ReLUs), and many other training techniques examples.

Application of DNNs are broadly expanded from tasks including but not limited to speech, and image recognition Deng et al. (2013); Krizhevsky et al. (2012), weather or climate studies Hayatbini et al. (2019b); Akbari Asanjan et al. (2018); Vandal et al. (2017); Tao et al. (2017); Liu et al. (2016); Xingjian et al. (2015); Tao et al. (2016), autonomous driving Chen et al. (2015), medical applications Esteva et al. (2017), game theories Silver et al. (2016) and etc. Deep Learning (DL) algorithms have gained significant popularity for many applications in the field of remote-sensing Zhang et al. (2016); Zhu et al. (2017); Chen et al. (2014).

Some commonly used DL models in remote sensing include Convolutional neural networks, Recurrent neural networks, Autoencoders (AEs) and stacked autoencoders, and Generative adversarial networks that will be introduced in the remainder of this section.

Convolutional Neural Networks (CNNs) consist of convolution layers, pooling layers and fully connected layers to better process multiple arrays of data LeCun et al. (2015). For this reason, CNNs are popular tools to analyze multi-band remote-sensing image data. The input image is convolved using a set of K kernels $W = \{W_1, W_2, \dots, W_k\}$ and added biases $\gamma = \{b_1, \dots, b_k\}$ to aggregate the values of pixels within a neighborhood using the max or mean operation. A new feature map X_k is generated for each convolutional layer

$$l : X_k^l = \sigma(W_k^{l-1} * X^{l-1} + b_k^{l-1}). \quad (2.1)$$

Where $\sigma(\cdot)$ is the element-wise nonlinear transform that X_k is subjected to Ma et al. (2019).

Some popular CNN architectures include but not limited to ALEXNET Krizhevsky et al. (2012), VGG NETWORKS (Simonyan, Zisserman, 2014), RESNET (He et al., 2016), Inception-v4 (Szegedy et al., 2017).

Recurrent Neural Networks (RNNs) are widely used for sequential inputs. This capability is due to a memory that is used to learn and store long-term dependency and information (Bengio et al., 1994). long short-term Memory cell (Hochreiter, Schmidhuber, 1997) and gated recurrent unit (Cho et al., 2014) are the examples of developed memory units. RNNs have extensively applied on remote-sensing images for a variety of tasks (Minh et al., 2018; Mou et al., 2017; Ienco et al., 2017; Lyu et al., 2016).

Autoencoders (AEs) consist of multiple layers of stacked AE layers, and the output of each

layer is connected to the input of the following layer. They map the input to a latent representation through one hidden layer with smaller number of hidden units than the input or output (Zhu et al., 2017). This network is widely used for the processing of feature hierarchy and has been implemented in the field of remote-sensing for the feature representation task (Wang et al., 2018; Abdi et al., 2017; Hao et al., 2017; Chen et al., 2017; Gong et al., 2017).

Generative Adversarial Networks (GANs) (Goodfellow et al., 2014) are a popular category of unsupervised models. The GAN is built of two networks competing with each other: a generative network (generator) and discriminative network (discriminator). The generator learns to map from a particular data distribution, and the discriminator tells the difference between the real data and the generated data produced by the generator. These two networks keep fooling each other by generator producing more realistic examples and the discriminator by better detecting the real from generated examples. Both networks try to optimize a loss function in a zero-sum game (Oliehoek et al., 2017). GANs have been popular in many computer vision and image processing applications (Isola et al., 2017; Hayatbini et al., 2019b; Lin et al., 2017; Zhan et al., 2018).

Chapter 3

Cloud Detection and Segmentation from Multi-spectral Satellite Information

3.1 Introduction

The purpose of this study is to improve the state-of-the-art version of PERSIANN-CCS (Precipitation Estimation from Remotely Sensed Information using Artificial Neural Network-Cloud Classification System) to support the NASA's Integrated Multi-Satellite Retrievals for Global Precipitation Measurement (IMERG) algorithm of the Global Precipitation Measurement (GPM) mission for near real-time monitoring of global precipitation at $0.1^\circ \times 0.1^\circ$ resolution over the chosen domain of 50N to 50S with 30 minutes time intervals (Huffman et al., 2015).

This study is motivated by the recognition of the disadvantages of threshold-based segmentation techniques for patch-based precipitation retrieval algorithms as discussed in chapter 2. We introduce a mathematical morphology-based method that integrates the complemen-

tary multi-spectral information from the gradient magnitudes of satellite images and is a well fit in the context of PERSIANN-CCS segmentation algorithm. This Gradient-based Multi-spectral Segmentation (GMS) algorithm comprises of several approaches that have been developed to extract various types of clouds including warm clouds. In this study, the algorithm is applied to model simulated GOES-16 ABI imagery. The simulated radiances for different channels of GOES-16 ABI along with the accompanying model simulated horizontal distribution of all clouds hydrometeors are used as the reference to validate the proposed algorithm in detecting and segmenting clouds.

Although the GMS algorithm is applied to geostationary satellite imageries in this study, it can be extended to other types of satellite dataset as well. This study will be the first step toward the ultimate goal which is precipitation estimation from remotely sensed information. In section 3.2, we explain the consisting steps of the developed GMS algorithm. Description of dataset and the case studies used in the study are described in section 3.3. Results and evaluation using both statistical scores and visual analyses are provided in section 3.4. Lastly, the conclusions of this study are presented in section 3.5.

3.2 Methodology

3.2.1 GMS Framework for Cloud Detection and Segmentation

The GMS algorithm is built on a hierarchical structure as the flow diagram shown in Fig. 3.1. This algorithm mainly carries out the following steps: multi-scale gradient magnitude computation, markers generation, and watershed segmentation. They will be explained in the following subsections.

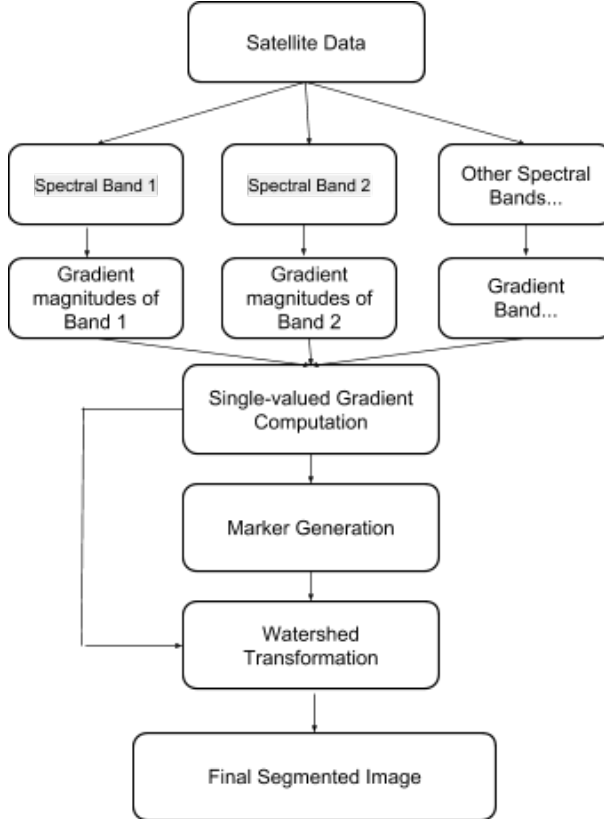


Figure 3.1: Flow diagram of the proposed multi-spectral gradient-based segmentation algorithm.

Multiscale Gradient Magnitude Computation

Gradient computation here means identifying the maximum change of each pixel's intensity in the neighborhood. The gradient highlights the sharp changes in intensity or the edges in an image. In a grayscale morphology, the gradient can be attained by subtracting the eroded image from the dilated image using a structuring element (Soille, Pesaresi, 2002). Gray-scale image pixels' value can be represented with the x and y coordinates as a three-dimensional set (Parvati et al., 2008). With this concept, gray-scale dilation can be defined as follows:

Let $f(s, t)$ represent an image and $B(x, y)$ be the structuring element. The structuring element (kernel) is a group of pixels of different sizes and shapes. In this study, a flat kernel, which means a squared window of pixels with equal weights, is considered for simplicity.

Gray-scale dilation of f by B is defined as below:

$$(f \oplus B)_{(s,t)} = \text{Max} \left\{ f(s-x, t-y) + B(x, y) \mid (s-x), (t-y) \in D_f; (x, y) \in D_B \right\} \quad (3.1)$$

Gray-scale erosion of f by B is defined as below:

$$(f \ominus B)_{(s,t)} = \text{Min} \left\{ f(s+x, t+y) - B(x, y) \mid (s+x), (t+y) \in D_f; (x, y) \in D_B \right\} \quad (3.2)$$

where D_f and D_B are the domains of f and B , respectively. The conditions that $(s+x)$ and $(t+y)$ have to be in the domain of f and (x, y) have to be in the domain of B is equivalent to the condition in the binary description of dilation and erosion. Two sets have to at least share one pixel in common in dilation, however, the structuring element has to be completely contained by the set being eroded in erosion (Pahsa, 2006). For further details on the erosion and dilation operations please refer to Gonzalez, Woods (1992).

The gradient image is calculated using equation (3.3) below from the original image, and it corresponds to the sharpness of the intensity change for each pixel (Parvati et al., 2008):

$$\text{MG}(f) = (f \oplus B) - (f \ominus B) \quad (3.3)$$

A multi-scale gradient algorithm capable of utilizing a varying scale-structuring element in mathematical morphology is implemented to reduce the sensitivity to noise and to extract various finesses of the edges of the objects in remote sensing images (Wang, 1997):

$$\text{MG}(f) = \frac{1}{n} \sum_{i=1}^n [((f \oplus B_i) - (f \ominus B_i)) \ominus B_{i-1}] \quad (3.4)$$

Where B_i denotes the group of square structuring elements with the size of $(2i+1) \times$

$(2i + 1)$ pixels and n is the scale which in this study is set to value of 5. Component-wise and vector-based strategies can be used to extend mathematical morphology from a single-channel grayscale image to a multichannel image (?). Component-wise strategy processes each channel of the multispectral image separately, while the vector-based strategy uses a vector approach to process the multispectral channels all at once (?). In this study, the component-wise approach is used for multispectral gradient image computation, since it is easy to implement and the results are satisfying. The morphological gradient is calculated separately for each band, and the resulting gradient image values are combined via equal weighted summation to generate a single gradient image to represent different channels. This way the gradient values can be obtained by summing up the complementary measurements from multiple channels of satellite imagery.

$$\text{MG}(f) = \sum_{i=1}^n MG(f_i) \quad (3.5)$$

Marker Generation and Local Minima Elimination

Markers are the selected regional minima of the input image, which are being used before watershed transform. The reason to employ so-called markers is to reduce redundant catchment basins due to the high sensitivity of the watershed transformation algorithm to noise and irrelevant local minima. The generation of pertinent markers is important to the successful application of watershed segmentation (Soille, Pesaresi, 2002).

The markers are either single points or regions that are placed inside objects of interest (Parvati et al., 2008). In this study, we generated markers through automatic thresholding of gradient magnitudes. Clusters of image pixels are classified as seed or non-seed pixels using the Otsu thresholding method (Otsu, 1979), which automatically selects an optimal

threshold based on maximizing the separability of the group-wise pixel values in grey levels, to generate the marker image. It selects a satisfactory threshold level to extract objects from their background based on a gray-level histogram. The reason to implement this method is based on the histogram plot of the gradient magnitudes shown in figure 3.2 that gradient magnitudes of most pixels are confined to the lower value range, while the sharp edge pixels with large gradient magnitudes are greater and separable from those within the background. For further explanation of this thresholding method and examples, one can refer to Otsu (1979) and Zhang et al. (2014).

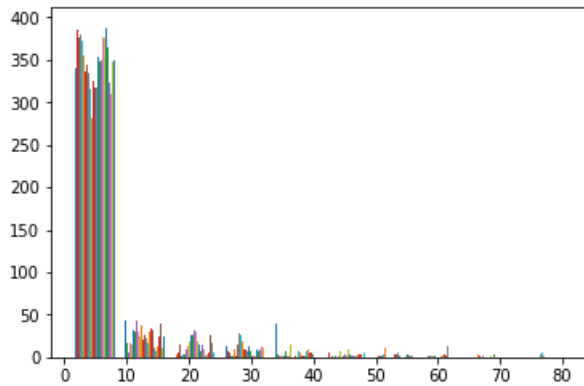


Figure 3.2: Histogram plot of the gradient magnitude image. Horizontal axis is showing the range of gradient magnitude values, and the vertical axis is the number of pixels with each gradient magnitude value.

Watershed Segmentation on the Gradient Images

The watershed transformation (Vincent, Soille, 1991) is a powerful segmentation algorithm from mathematical morphology and has been used in many segmentation problems (Hsu et al., 2010; Zahraei et al., 2013; Lakshmanan et al., 2009). This approach is usually applied to satellite images to extract regions (i.e., objects) that are identified as clouds. The basic idea of the watershed algorithm is to consider the single channel image as a three-dimensional topography map where the lower values are considered as valleys (local minima) and the higher values are assumed to be hills. Each local minimum is then flooded to neighboring

pixels until meeting an adjacent catchment. A ridgeline is then delineated along any two regions' borders, hence the catchment basins are delimited by watershed lines (Fig. 3.3). Further information about the watershed segmentation algorithm can be found in Vincent, Soille (1991).

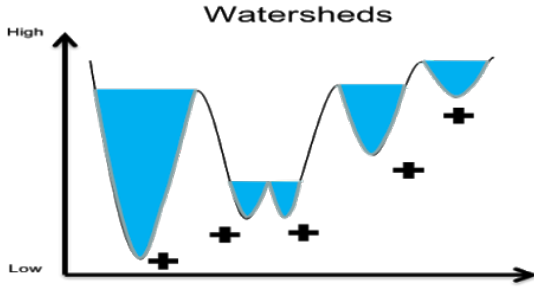


Figure 3.3: Watershed Transformation Process Diagram. Each of the positive signs represents one watershed domain.

The morphology-based watershed transformation used in this study is applied to the gradient magnitude of satellite images. This is different from the traditional segmentation used in PERSIANN-CCS algorithm that the watershed transformation is directly applied on temperature values lower than a predefined threshold. Applying transformation on gradient images can capture warm clouds without dependency on predefined temperature thresholds as a controlling factor. Fig. 3.4A demonstrates how local minima associated with warmer cloud regions will be disregarded by a predefined threshold applied to the values before implementing the watershed algorithm. Increasing the temperature threshold in order to capture the clouds with the higher temperature values (Fig. 3.4B) results in merging the local minima which are representative of distinct clouds and causes misleading outcomes. Optimal results are achieved when the watershed algorithm is applied to the gradient magnitude images that delineate the boundaries of all types of clouds, regardless of their height or temperature. In Figure 3C, high gradient magnitude values are representative of pixels with sharp intensity transitions or cloud boundaries. Hence, the catchment basins are described as regions between any two local maximum of the gradient magnitudes.

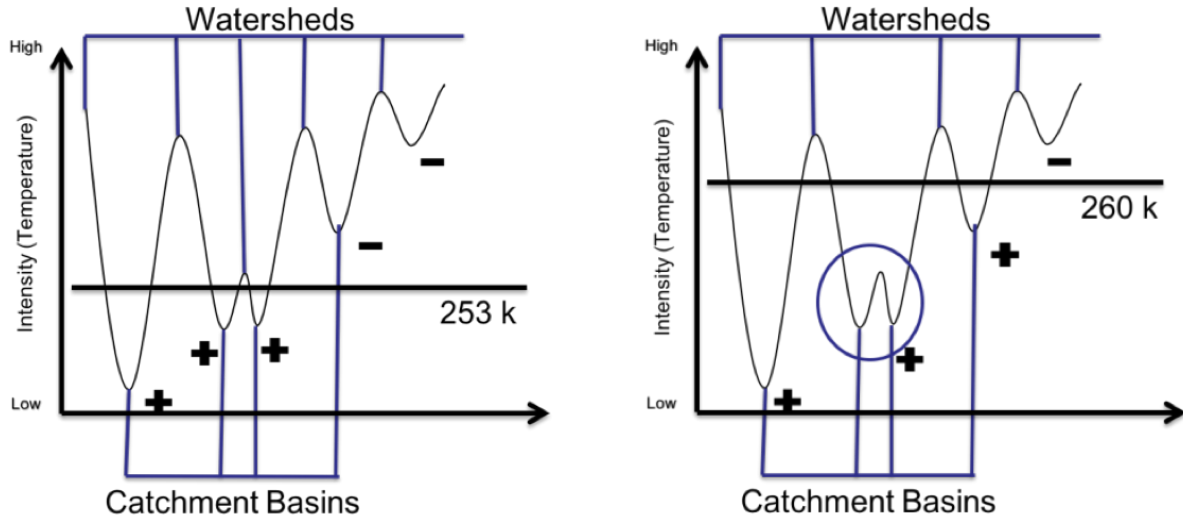


Figure 3.4: Effect of increasing the threshold on the Watershed segmentation technique. The positive (negative) signs are representing the seeds that are included (excluded) in the segmentation process.

3.3 Description of the Dataset

3.3.1 GOES-16 ABI

The primary data sets collected and processed in this research include different channels of geostationary weather satellite bands of GOES-16. The Advanced Baseline Imager (ABI; Schmit et al., 2005) onboard GOES-16 can provide more accurate, detailed, and timely detection of high-impact environmental phenomena by more spectral channels (2 visible, 4 near-infrared and 10 infrared channels), and higher spatial ($2 \text{ km} \times 2 \text{ km}$ at nadir for infrared channels) and temporal (every 5 minutes for CONUS) resolutions over its predecessors. The development of the ABI is being done as a collaborative effort between the National Aeronautics and Space Administration (NASA) and NOAA. For readers interested in further details, Schmit et al. (2005) is considered as the references.

3.3.2 PSU WRF-EnKF Dataset

We used two simulated cases to examine the performance of the proposed algorithm. Both two simulations are generated using the Weather Research and Forecasting (WRF) model with its Advanced Research WRF (ARW) dynamical core (Skamarock et al., 2008), with initial conditions generated by the WRF-based ensemble Kalman filter (EnKF) data assimilation system developed at the Pennsylvania State University (Zhang et al., 2009, 2011).

The first case study is a simulation of hurricane Harvey (2017) which brought record-breaking catastrophic rainfall in southern Texas. Harvey is the second costliest hurricane in history, just below hurricane Katrina (2005), and it is also the first storm that was fully captured by GOES-16. The simulation utilized version 3.6.1 of the WRF model with a 3-km horizontal resolution. After assimilating brightness temperature observations from ABI every one hour for several cycles, deterministic forecast is initialized from the EnKF analysis at 0600 UTC 23 August 2017. For the purpose of this study, we only used simulated brightness temperature of the model outputs of a one-day period from 0000 UTC 26 August to 0000 UTC 27 August, right after Harvey made its landfall. Further details of the simulation of hurricane Harvey, including verifications of its track, intensity, and cloud forecasts with observations can be found in Zhang et al. (2019).

The second case is a simulation of tornadic supercell thunderstorms across Wyoming, Nebraska and Colorado on 12 June 2017, which is one of the first severe thunderstorm event captured by GOES-16. The simulation utilized version 3.8.1 of the WRF model with a 1-km horizontal resolution. Brightness temperature observations from ABI are assimilated every 5 minutes, and deterministic forecast is initialized from EnKF analysis at 2000 UTC, 12 June 2017, when the thunderstorms were just initiated. The simulations were carried out till 0000 UTC, 13 June 2017, with outputs every 5 minutes. Further details of the simulation of this severe thunderstorm event and the verifications of the thunderstorm predictions with the

observations can be found in Zhang et al. (2018).

These two cases differ significantly in the strength and size of clouds. The tornadic supercell thunderstorm case is one of the smallest organized cloud systems and occur mostly over the mid-latitude continents, while hurricanes have the largest and most expansive cloud systems originated from the tropical oceans. We can examine the strength and flexibility of the proposed algorithms using these two distinctive situations to see if it can detect diverse types of clouds effectively by utilizing fixed parameter values.

3.4 Results and Discussion

Experiments are carried out to validate the GMS algorithm by applying it to the model simulated GOES-16 ABI imageries, and compare with accompanying synthetic cloud mask from the horizontal distribution of all cloud hydrometeors known as the ‘ground truth’.

Visual comparisons and statistical evaluations are performed for both cases to obtain the accuracy of the proposed segmentation algorithm in comparison to the single-channel, threshold-based segmentation approach that is currently in use for PERSIANN-CCS. Although the GMS algorithm is capable of integrating information from different spectral bands, the results shown in this section are obtained from single-band IR cloud top brightness temperature in order to be consistent with the PERSIANN-CCS single-band segmentation algorithm.

3.4.1 Visual Comparison

The final gradient-based segmentation results from simulated IR input along with gradient magnitude imageries of hurricane Harvey and the Wyoming thunderstorm event are shown in Fig 3.5 and 3.6, respectively. The gradient magnitudes are calculated from the IR images and

the watershed segmentation is then applied to the gradient magnitude imageries based on the generated markers to achieve the final cloud patch segmentation. Fig 3.5A and 3.6A, presents a simulated IR longwave window band from GOES-16 ABI (The scale bar is temperature in degree Kelvin). Fig 3.5B and 3.6B, presents normalized gradient magnitudes imagery for the corresponding Simulated IR Channel (Scale bar is normalized gradient magnitude values). Fig 3.5C and 3.6C, presents resulting cloud Segments (Each random color represents a distinct segment).

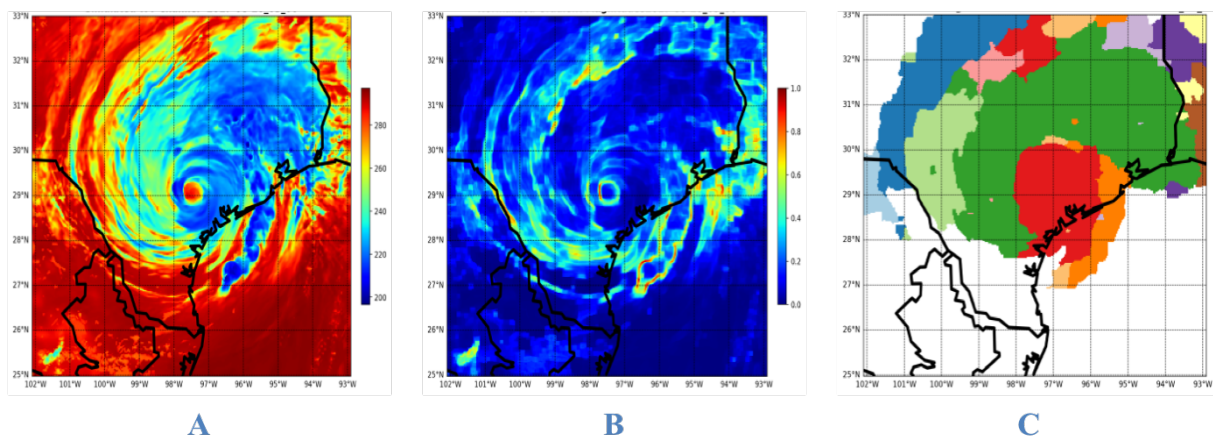


Figure 3.5: Visualization of the gradient based segmentation result for simulated Hurricane Harvey event on August 26th 2017 at 3:00 AM UTC.

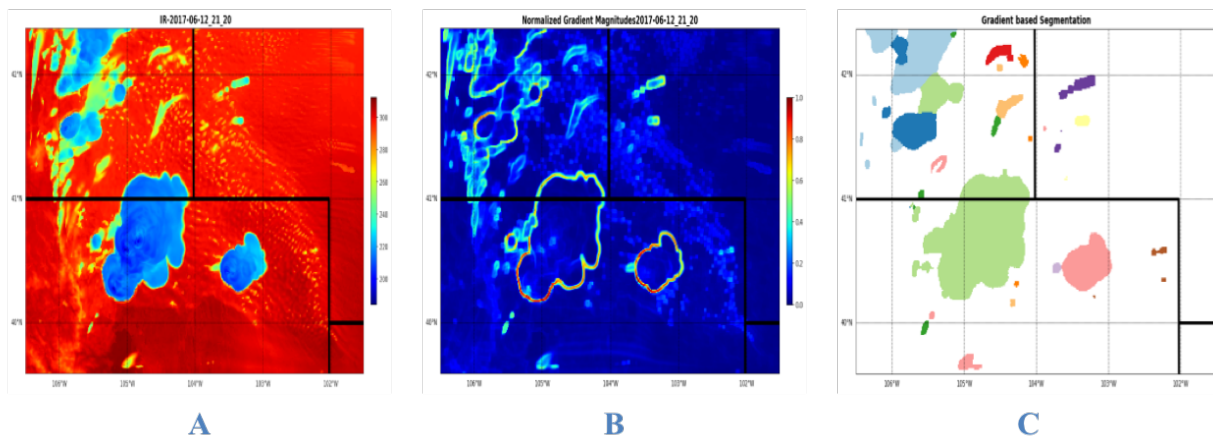


Figure 3.6: Visualization of the gradient based segmentation result for the simulated Wyoming tornado event at 21:20 UTC of the 12th of June 2017.

Fig 3.7 and 3.8 show that in both cases the newly developed algorithm can capture more clouds especially the warmer ones compared with the PERSIANN-CCS. This indicates that the gradient-based segmentation algorithm is capable of overcoming the drawback associated with threshold-based segmentation approaches implemented in patch-based precipitation retrieval algorithms. Fig 3.7A and 3.8A, presents 'Truth' Cloud Mask used as a reference. Dark blue region is implying the cloud existence. Fig 3.7B and 3.8B, presents PERSIANN-CCS segmentation result from single-IR channel. Fig 3.7C and 3.8C, presents gradient-based segmentation algorithm output based on only IR channel. In panels B and C each random color identifies a distinct cloud patch.

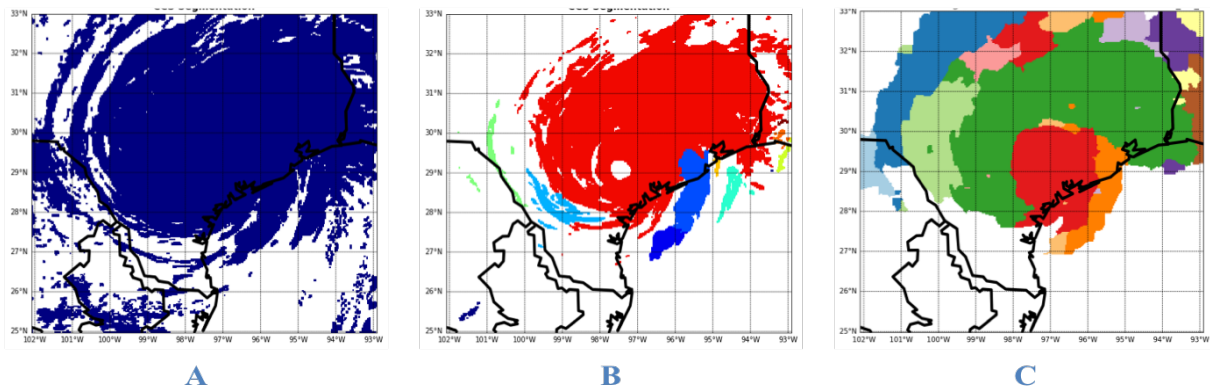


Figure 3.7: Visual comparison of the two segmentation output (B and C) based on the 'truth' mask as a reference for the simulated Hurricane Harvey event at 3:00 AM UTC of August 26th 2017.

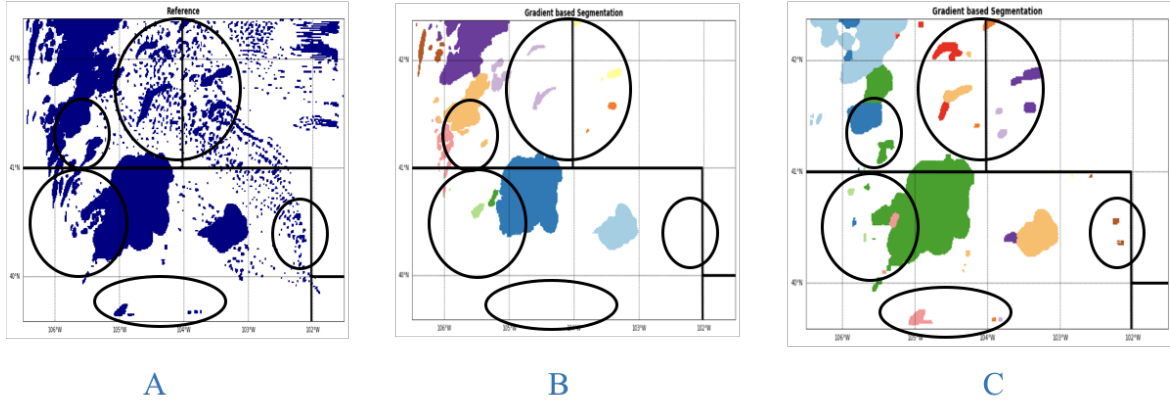


Figure 3.8: Visual comparison of the two segmentation output (B and C) based on the 'truth' mask as a reference for the simulated Wyoming tornado event at 21:20 UTC of the 12th of June 2017.

As mentioned in the methodology section, the gradient-based segmentation algorithm is capable of taking into account the complementary measurements from multiple channels. In order to visually assess the effect of integrating information from other spectral bands, channel 8 (lower-tropospheric water vapor channel) of GOES-16 ABI is also processed and gradient magnitudes are calculated separately for this band. The gradient values from each spectral bands are then summed up to generate a single-valued multispectral gradient magnitude image. The watershed segmentation is then applied to the combined gradient magnitude imagery.

The segmentation results from each scenario (IR-only, and IR+ Water vapor) are shown in Fig. 3.9 implying that integration of measurements from other spectral bands will provide useful information for distinct delineation of the clouds and helps to discard cloud patches that are mistakenly detected due to the background noise in the utilization of single channel data. Adding additional channels provides useful information for better defining the cloud segments and leads to a more accurate classification as the next step toward more robust intensity estimation and areal delineation of rainfall. Panels in section A Fig. 3.9 are showing final cloud segments from the gradient magnitudes of lower water vapor band.

Panels in section B are showing final cloud segments from the gradient magnitudes of single IR longwave window band. Panels in section C are showing final cloud segments from the combined gradient magnitude image of both spectral bands (IR longwave window and water vapor band).

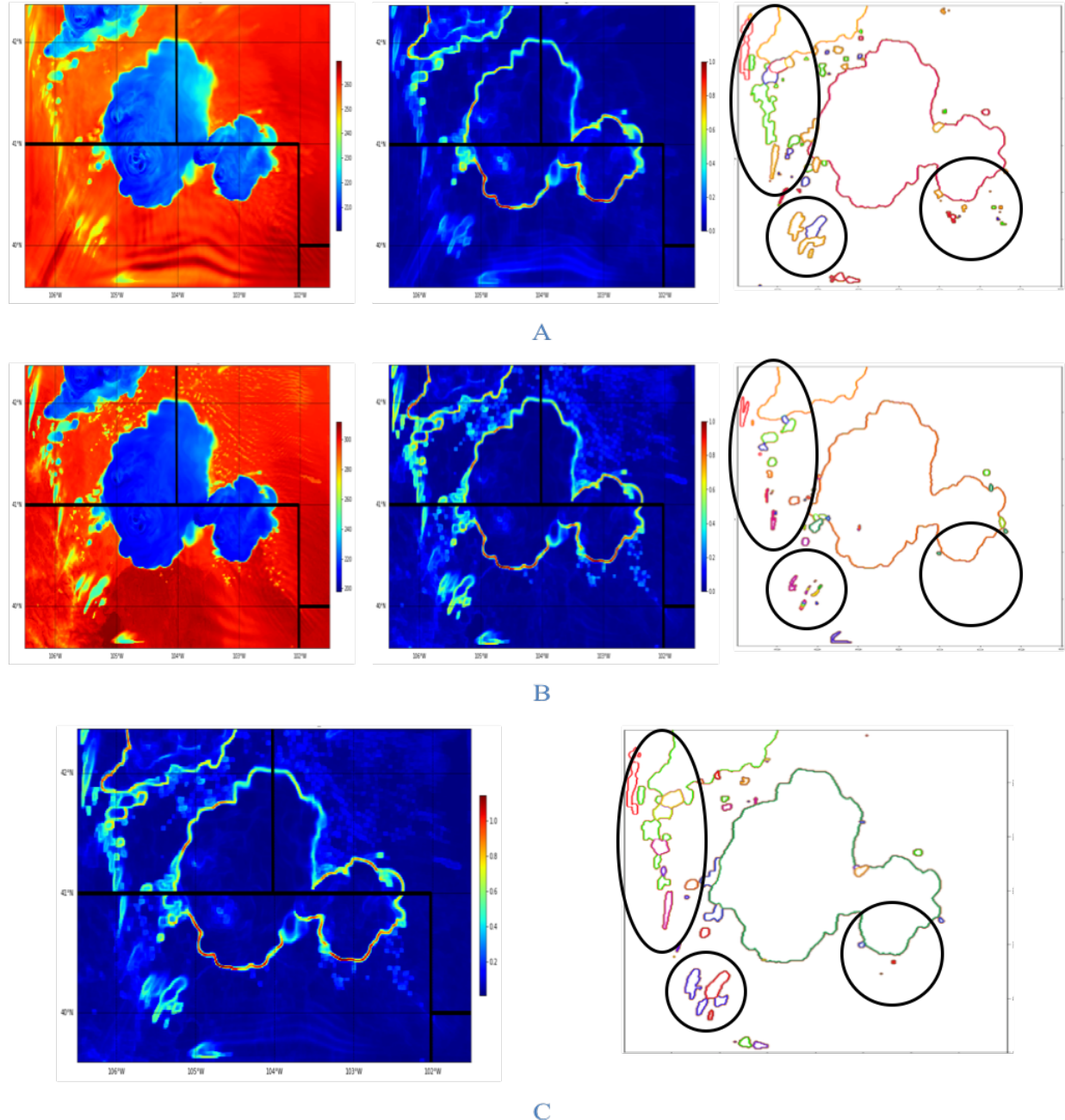


Figure 3.9: Visualizing the effect of integrating complementary information from lower-level water vapor for the Wyoming tornado case at 21:05 UTC of the 12th of June 2017.

3.4.2 Statistical Evaluation

A reference cloud mask is needed in order to perform an accuracy assessment and to compare the outcomes of the proposed segmentation algorithms. The model simulated mixing ratios combining all hydrometeors, including cloud water, cloud ice, rainwater, snow, and graupel, are used as ‘truth’ observation mask to determine whether a grid point is covered by cloud or not. These hydrometeor mixing ratios are prognostic model variables simulated by the microphysics scheme and evolve in correspondence with the dynamical and thermodynamical processes within the WRF model. After summing them all together and taking the vertical maximum value within each column, a threshold of $10e^{-6}$ kg kg $^{-1}$ is applied to the horizontal hydrometeor mixing ratio map. This value is a widely-used threshold for cloud top and cloud base identification from model simulations beginning from Otkin, Greenwald (2008). The grid point is cloudy if hydrometeor mixing ratio at this location is greater than the threshold and is clear sky if it is lower than the threshold. The model-derived horizontal distribution of clouds is used as the “truth” to verify and compare the two different cloud identification algorithms. The situations of whether the segmentation algorithm detects the clouds successfully or not are shown with the verification indices used along with their application listed in Table 3.2.

Table 3.1: The four possible diagnosis results of testing.

	Detected	Not detected	Probability
Existing	True positive (TP) The existing defect is detected (hit)	False negative (FN) The existing defect is not detected (miss)	TP + FN = 100 %
Non-existing	False positive (FP) Defect is detected but not exists (False Alarm)	True negative (TN) No defect is detected, no defect exists (Correct Rejection)	FP + TN = 100 %
Total	FP + TP	FN + TN	Total = TP + FN + TN + FP

Table 3.2: Verification Metrics

Verification Metrics	Formulation	Range	Application
Undetected Error Rate	$Ur = \text{Misses}/\text{Number of observed events}$	$(0 \leq Ur \leq 1)$ Perfect score: 0	The rate of error in detection of hit events
Probability of Detection	$POD = \text{Hits}/\text{Number of observed events}$	$(0 \leq POD \leq 1)$ Perfect score: 1	The likelihood of correct detection
False Alarm Ratio	$Fr = \text{False Alarm}/\text{Number of Not Observed Events}$	$(0 \leq Fr \leq 1)$ Perfect score: 0	The number of false alarms per total number of alarms
Bias Score	$\text{Bias} = (\text{Hits} + \text{False alarms}) / \text{Number of observed events}$	$(0 \leq BI)$ Perfect score: 1	How similar were the frequencies of Existing and Detected events?
Equitable Threat Score (ETS)	$ETS = \text{Hits} - \text{Hits}_{\text{random}} / (\text{Hits} + \text{Misses} + \text{False alarms} - \text{Hits}_{\text{random}})$	$(-1/3 < ETS < 1)$ Perfect score: 1	How well did the Existing events correspond to the Detected events

Constant improvements in segmentation skill using the GMS algorithm is evident for both events with their cloud systems evolve considerably in structure and morphology (Fig. 3.10, 3.11). The improvement is pronounced when only IR data are used to keep the consistency between the proposed segmentation algorithm and the one used in PERSIANN-CCS. The only metric that is not showing the performance enhancement is the False Alarm Ratio (FAR; with the best score of zero), with non-zero but insignificant average value of 0.03 (Fig. 3.10 B, 3.11 B). This higher value of FAR is in compensation of the higher POD that we obtained in comparison to the PERSIANN-CCS segmentation algorithm. The conventional segmentation algorithm misses the clouds with higher temperatures than the manually set temperature threshold and only captures the colder clouds. Therefore, low or zero FAR is expected. The gradient-based segmentation algorithm, on the other hand, can cover both warm and cold clouds with potentially higher FAR.



Figure 3.10: Statistical comparison of two different segmentation algorithms for Hurricane Harvey case.

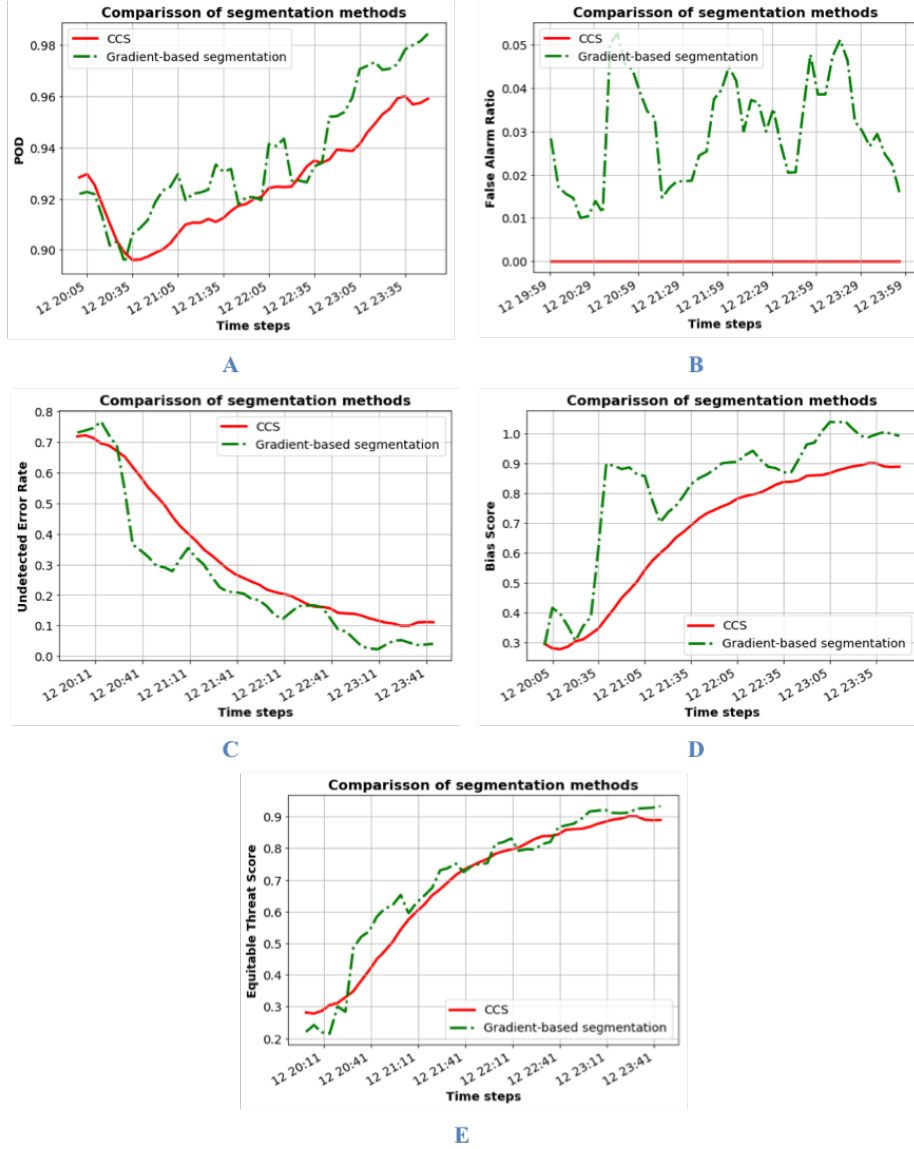


Figure 3.11: Statistical comparison of two different segmentation algorithms for Wyoming Tornado case.

3.5 Summary and Conclusions

A gradient-based multispectral segmentation algorithm for cloud detection and segmentation using satellite imageries is developed and presented. The goal is to provide a more effective and flexible method to overcome the shortcomings associated with the traditional

patch-based cloud segmentation approaches towards more reliable precipitation retrievals. This algorithm is based on mathematical morphology, and image processing techniques developed to extract information from single or multiple channels of satellite imagery. Due to the unique characteristics of each spectral band, accumulation of additional sources of information from multi-channel satellite imagery became viable by using the gradient magnitudes instead of directly utilizing each channel's values. This gradient-based cloud image segmentation method integrates morphological image gradient magnitudes to separable cloud systems and patches boundaries using a convolution operation. As a result, a wider range of cloud types regardless of their temperature and height can be detected and segmented. The proposed algorithm, as well as the conventional threshold-based segmentation approach used in the PERSIANN-CCS algorithm, are applied on the simulated GOES-16 ABI imageries from high-resolution numerical weather simulations accompanied with their modeled horizontal distribution of hydrometeors as the reference to examine their performance. Results from visual and statistical comparison indicate a constant improved performance of the gradient-based segmentation technique over the traditional approaches specifically in terms of extracting warm cloud regions. More accurate extraction of cloud patches provides the opportunity for a more effective cloud tracking towards dynamic analysis of precipitation estimation. This algorithm is the first step towards reducing the uncertainty associated with precipitation retrieval from remotely sensed information.

Chapter 4

Rain/Norain Detection and Rainfall Estimation from Multispectral Satellite Information

4.1 Introduction

Near-real-time satellite-based precipitation estimation is of great importance for hydrological and meteorological applications due to its high spatiotemporal resolution, and global coverage. The accuracy of precipitation estimates can likely be enhanced with implementation of the recent developments in technologies and data with higher temporal, spatial, and spectral resolution. Another important factor to more efficiently and accurately characterize these natural phenomena and their future behavior is the use of the proper methodologies to extract applicable information and exploit it in the precipitation estimation task (Sorooshian et al., 2011).

This study explores the application of the conditional GANs as a type of Generative Neural

Networks to estimate precipitation using multiple sources of inputs including multispectral geostationary satellite information. This is an investigation for the development of an advanced satellite-based precipitation estimation product driven by state-of-the-art deep learning algorithms and using information from multiple sources. The objectives are to report on: 1) application of CNNs instead of fully connected networks in extracting useful features from GEO satellite imagery to better capture the spatial and temporal dependencies in images, 2) demonstrating the advantage of using more sophisticated loss function to better capture the complex structure of precipitation, 3) evaluating the performance of the proposed algorithm considering different scenarios of multiple channel combinations and elevation data as input, and 4) evaluate the effectiveness of the proposed algorithm by comparing its performance with PERSIANN-CCS as an operational product and a baseline model with a conventional type of loss function. The remainder of this section is organized as follows. Section 4.2 briefly describes the study region and the datasets used for this study. Section 4.3 explains the methodologies and details about the experiments in each step of the process. Section 4.4 presents the results and discussion and finally, section 4.5 discusses the conclusions.

4.2 Materials and Study Region

The primary data sets used in this research include different channels and combinations of bands from the Advanced Baseline Imager (ABI) onboard GOES-16 (NOAA/NASA). GOES-16 is the next generation of the Geostationary Operational Environmental Satellite (GOES) with the Advanced Baseline Imager (ABI; Schmit et al., 2005), with 16 channels. Compared to five spectral bands available on the preceding generations of GOES, the ABI provides four times higher spatial resolution, and almost five times faster temporal coverage than the previous system. Providing much greater detail, ABI enables more accurate monitoring of weather and climate. Each of the bands from GOES satellite is most sensitive to a

certain part of clouds and will give a better insight on structure, and properties of cloud patches and might have different applications. In this study, the emissive bands of GOES-16 satellite with approximate central wavelengths of 3.9, 6.18, 6.95, 7.34, 8.5, 9.6, 10.35, 11.2, 12.3, 13.3 μm are implemented due to their continuous availability both for daytime and nighttime. The data covers the time period from 2017 to the present at the temporal resolutions of 30 seconds to 15 minutes and are hosted by NOAA’s Comprehensive Large Array-data Stewardship System. More information about GOES-16 can be found in Schmit et al. (2010).

The target data in this study is the National Severe Storms Laboratory (NSSL) Multi-Radar Multi-Sensor (MRMS) system which is developed by NSSL and recently activated by NOAA’s National Weather Service (NWS). MRMS data is obtained from GPM Ground Validation Data Archive. In this work, the MRMS data is processed to be used over the United States (24.35° to 49.1° N, -124.4° to -66.7° W) for every 30 minutes with 4 km spatial resolution in order to match with PERSIANN-CCS product. To keep the consistency of the nadir spatial resolution of the ABI channels and MRMS data implemented in this study with the PERSIANN-CCS operational product all the measurements mapped to the same resolution of 4 km. In our experiments, we also include elevation data from the Global 30 Arc-Second Elevation Data Set (GTOPO30) provided by the USGS (Danielson, Gesch, 2011).

4.3 Methodology and Model Setup

With the constellation of a new generation of satellites, an enormous amount of remotely sensed measurements is available. However, it is still a challenge to understand how these measurements should best be used to improve the precipitation estimation task. Specifically, here we explored the application of CNNs and GANs in step-by-step phases of our experiment to provide a data-driven framework for near real-time precipitation estimation. Figure 4.1

illustrates an overview of our framework, which consists of three main components: data pre-processing, deep learning algorithms, and evaluation.

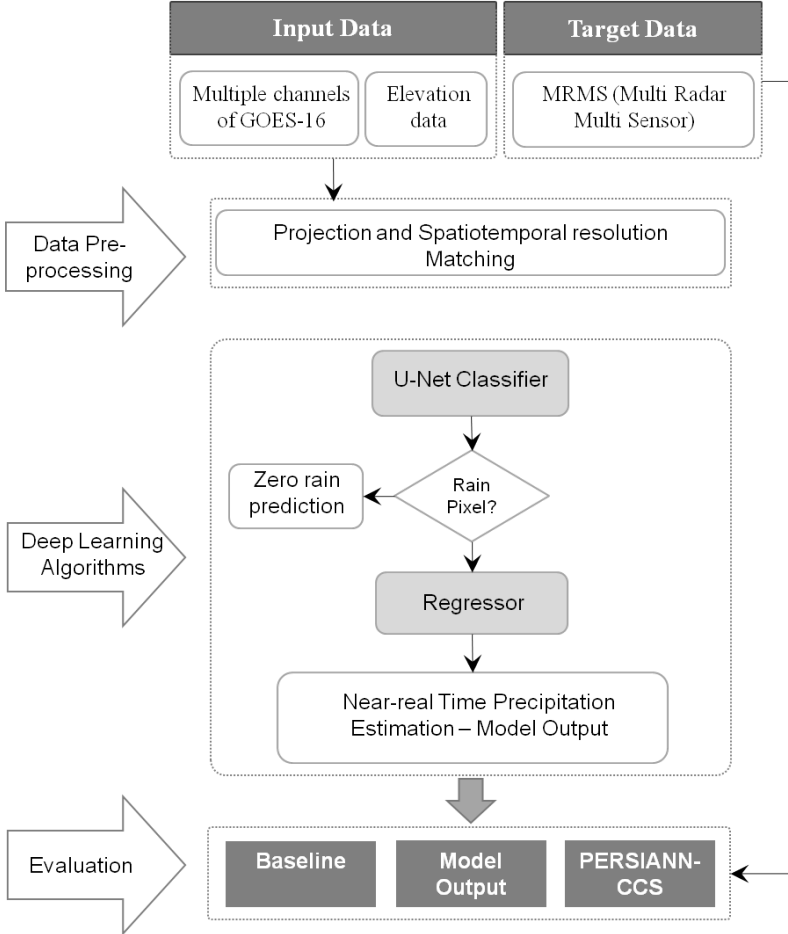


Figure 4.1: The proposed framework for the Precipitation Estimation.

Data pre-processing is an essential part of our framework as measurements collected from different spectral bands have different value ranges. For example, $0.86 \mu\text{m}$ ("reflective") band contains measurements ranging from 0 to 1 while $8.4 \mu\text{m}$ ("cloud-top phase") band contains measurements ranging from 181 to 323. Normalizing the input is common practice in machine learning as models tend to be biased towards data with the largest value ranges. We make the assumption that all remotely sensed measurements are equally important, so we normalize the data of each channel to range from 0 to 1. Observations of each channel are normalized using the parameters as shown in Table 4.1, by subtracting the min value

from the channel value and dividing by the difference between the min and max values. Moreover, all the datasets are matched in terms of spatiotemporal resolution to qualify for image-to-image translation. As a result, both the MRMS and imageries from GOES-16 were up-scaled to match the PERSIANN-CCS as the baseline with 30 minutes temporal and 4 km by 4km spatial resolution.

Table 4.1: Parameters for channel normalization applied using the formula: $\frac{value - \min}{\max - \min}$

Band Number - Wavelength (μm)	min	max
8 – 6.2	187	260
9 – 6.9	181	270
10 – 7.3	171	277
11 – 8.4	181	323
13 – 10.3	181	330
14 – 11.2	172	330

The pre-processed data is then used as input for deep learning algorithms. In this study, we explore the application of CNNs to learn the relation between input satellite imagery and target precipitation observations. Specifically, we use the U-net architecture that has become popular in recent years in the computer vision—with applications ranging from image-to-image translation to biomedical image segmentation. An illustration of the U-net architecture is presented in Figure 4.2, which shows an encoder-decoder network but with additional ”skip” connections between the encoder and decoder. The bottle-necking of information in the encoder helps capture global spatial information, however, local spatial information is lost in the process. The idea behind the U-net architecture is that decoder accuracy can be improved by passing the lost local spatial information through the skip connections. Accurately capturing local information is important for precipitation estimation as rainfall is generally quite sparse—making pixel-level accuracy that much more important. For more information regarding U-nets please refer to Ronneberger et al. (2015).

U-net is used to extract features from the pre-processed input data, which are then used to

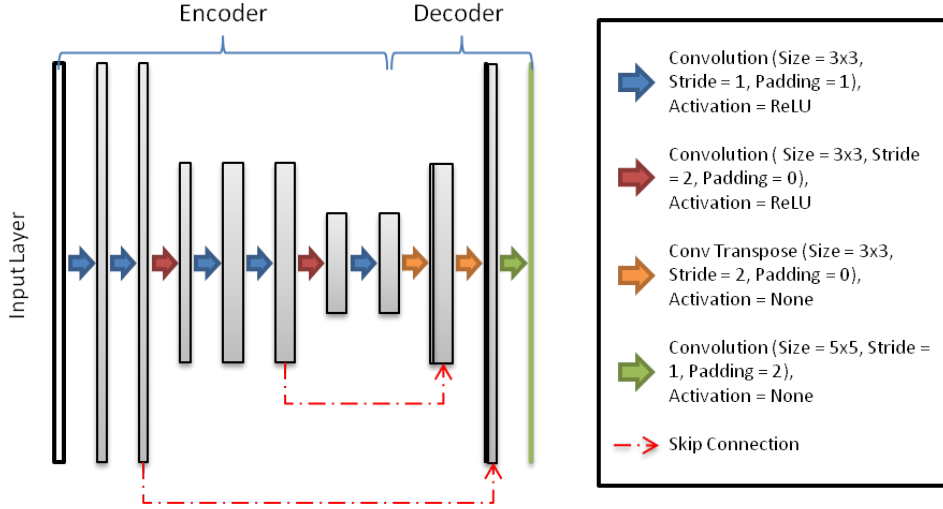


Figure 4.2: Visualized structure of U-net network.

predict the quantity of rainfall and the classification of rain/no-rain for each pixel. Each extracted feature is the same height and width as the input and target data, and is a single channel; the number of channels was selected through separate cross-validation experiments not discussed in this study. The single channel feature is then fed into a shallow regression network that predicts a quantity of rain for each pixel. The specific details of each network are shown in Table 4.2. In this table, each layer of the encoder feeds sequentially into the next layer, from top to bottom (i.e., "conv1" top, so the output of the "conv7" layer feeds into the "convt1" layer. Additionally, "convt2" and "conv8" layers take not only as input the output from their previous decoder layers, but also concatenates the output of the encoder layer of the same row (skip connection). This means the input of the "convt2" layer is the concatenated outputs of the "conv5" and "convt1" layers. The output of the "conv8" layer is the input for the classifier and regressor. C represents number of input channels.

Performance verification measurements for precipitation amount estimation and rain/no-rain (R/NR) classification are presented in Table 4.3 and Table 4.4 respectively. TP denotes the number of true positive events, MS denotes the number of missing events, FP denotes the number of false-positive events, TN denotes the number of true-negative events.

Table 4.2: Details of network architectures.

Feature Extractor								
Encoder				Decoder				
layer	kernel size, stride, padding	activation	batch norm	layer	kernel size, stride, padding	activation	batch norm	
conv1	$3 \times 3 \times C \times 64, 1, 1$	ReLU	Yes					
conv2	$3 \times 3 \times 64 \times 64, 1, 1$	ReLU	Yes	conv8	$5 \times 5 \times 65 \times 1, 1, 2$	None	No	
conv3	$3 \times 3 \times 64 \times 64, 2, 0$	ReLU	Yes					
conv4	$3 \times 3 \times 64 \times 128, 1, 1$	ReLU	Yes					
conv5	$3 \times 3 \times 128 \times 128, 1, 1$	ReLU	Yes	convt2	$3 \times 3 \times 129 \times 1, 2, 0$	None	No	
conv6	$3 \times 3 \times 128 \times 128, 2, 0$	ReLU	Yes					
conv7	$3 \times 3 \times 128 \times 128, 1, 1$	ReLU	Yes	convt1	$3 \times 3 \times 128 \times 1, 2, 0$	None	No	
Classifier				Regressor				
layer	kernel size, stride, padding	activation	batch norm	layer	kernel size, stride, padding	activation	batch norm	
conv1	$3 \times 3 \times 1 \times 1, 1, 1$	Sigmoid	No	conv1	$3 \times 3 \times 1 \times 1, 1, 1$	ReLU	No	

Table 4.3: Description of the verification metrics.

Verification measures	Formulas	Range and desirable value
Probability of Detection	$POD = \frac{TP}{(TP+MS)}$	Range: 0 to 1; desirable value: 1
False Alarm Ratio	$FAR = \frac{FP}{(TP+FP)}$	Range: 0 to 1; desirable value: 0
Critical Success Index	$CSI = \frac{TP}{(TP+FP+MS)}$	Range: 0 to 1; desirable value: 1

Two baselines are used to be compared to the output of our framework. The first one is the operational product of PERSIANN-CCS and the other one is a framework with the same structure as the proposed one, except that the loss term is calculated using only MSE. The reason to pick this baseline model is to show the superiority of the application of cGAN term in the objective function to better train the network for the task of precipitation estimation.

First phase of the methodology considers the most common scenario: one channel of IR from GOES-16 satellite is used as input to predict target precipitation estimates. In this phase, the networks in our framework (feature extractor and regressor) are trained using the mean squared error (MSE) loss, optimizing the objective:

$$\min_{G_{reg}} \mathbb{E}_{x,y \sim \text{Pr}} [\|y - G_{reg}(x)\|_2^2], \quad (4.1)$$

where Pr is the data distribution over real sample (x and y), G_{reg} is the feature extractor and

Table 4.4: Common verification measures for the satellite-based precipitation estimation products.

Verification measures	Formulas	Range and desirable value
Bias	$\text{Bias} = \bar{x} - \bar{y}$	Range: $-\infty$ to $+\infty$; desired value: 0
Mean Squared Error	$\text{MSE} = \frac{1}{N} \sum (x_i - y_i)^2$	Range: 0 to $+\infty$; desired value: 0
Pearson's Correlation Coefficient	$\text{COR} = \frac{\sum (x_i - \bar{x})(y_i - \bar{y})}{\sqrt{\sum (x_i - \bar{x})^2} \sqrt{\sum (y_i - \bar{y})^2}}$	Range: -1 to $+1$; desired value: 1

regressor, x is the input GOES satellite imagery, and y is the target precipitation observation. According to this phase experiments, the regressor predicts small quantities of rain when the target indicates no-rain pixels. Instead of deciding on an arbitrary threshold to truncate values with, we follow the work of Tao et al. (2018) and use shallow classification network to predict a rain/no-rain label for each pixel—a binary mask. Tao et al. (2018) applied Stacked Denoising Autoencoders (SDAEs) to delineate the rain/no-rain precipitation regions from bispectral satellite information. SDAEs are common and simple DNNs consisting of an autoencoder to extract representative features and learn from input to predict the output. The binary mask in our study is used to update the regression network’s prediction—pixels where the classification network predicts no-rain is updated to zero. The classifier uses the same single channel feature from the feature extractor as the regressor (details of the classifier are shown in Table 4.2). This gives us an updated objective of:

$$\min_{G_{reg}, G_{cls}} \mathbb{E}_{x,y \sim \mathbf{Pr}} [\|y - G_{reg}(x) \cdot G_{cls}(x)\|_2^2] + \mathbb{E}_{x,\hat{y} \sim \mathbf{Pr}} [\hat{y} \cdot \log(G_{cls}(x)) + (1 - \hat{y}) \cdot \log(1 - G_{cls}(x))], \quad (4.2)$$

where G_{cls} is the feature extractor and classifier and \hat{y} is the binarized version of y . Here the feature extractor in G_{cls} share the same weights as those in G_{reg} .

As mean squared error (MSE) is a commonly used objective for the task of precipitation estimation, we use it as our optimization objective in the first phase. Using MSE, however,

we find the outputs from precipitation estimators to be highly skewed toward smaller values due to the dominance of no-rain pixels, as well as, the rarity of pixels with heavy rain. This means that MSE by itself is insufficient in driving the model to capture the true underlying distribution of precipitation values. And since one of the main purposes of satellite-based precipitation estimation is to specifically track extreme events with negative environmental consequences, this behavior is problematic.

The second phase of our methodology looks to address this problematic behavior. We follow along the same line as Tao et al. (2018), who tried to remedy this behavior with the addition of a Kullback-Leibler (KL) divergence term to the optimization objective. KL divergence measures how one probability distribution p diverges from a second expected probability distribution q :

$$D_{KL}(p\|q) = \int_x p(x) \log \frac{p(x)}{q(x)} dx \quad (4.3)$$

D_{KL} achieves the minimum zero when $p(x)$ and $q(x)$ are equal everywhere. It is noticeable according to the formula that KL divergence is asymmetric. In cases where $p(x)$ is close to zero but $q(x)$ is significantly non-zero, then the effect of q is disregarded. This makes optimizing difficult when using gradient methods as there is no gradient to update parameters in such cases(Arjovsky et al., 2017).

We consider instead a different measure, the Jensen-Shannon (JS) divergence:

$$D_{JS}(p\|q) = \frac{1}{2}D_{KL}(p\|\frac{p+q}{2}) + \frac{1}{2}D_{KL}(q\|\frac{p+q}{2}) \quad (4.4)$$

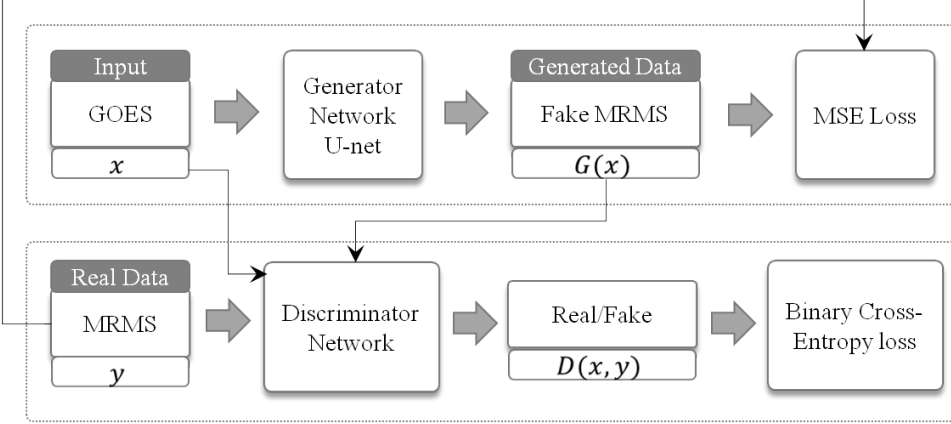


Figure 4.3: Schematic conditional Generative Adversarial Network Structure.

JS divergence is not only symmetric but is a smoother function compared to KL divergence, making it better suited to use with gradient methods. Huszár (2015) have demonstrated the superiority of JS divergence over the KL divergence for quantifying the similarity between two probability distributions. An implementation of JS divergence is a generative adversarial network (GAN), which adds a discriminator network that works against a generator network. The discriminator network discriminates whether the given input is a real sample from the true distribution (ground truth) or is a fake sample from a fake distribution (output from the generative network), and the generator network attempts to fool the discriminator. The GAN concept is illustrated in Figure 4.3, where G is a generator network and D is a discriminator network. For further detail on GANs structure please refer to the papers by Goodfellow et al. (2014) and Goodfellow (2016).

In our setup, the generator consist of the previously mentioned networks (feature extractor, classifier, and regressor), and a fake sample is an output from the regressor that has been updated using the binary mask from the classifier. Updating Eq. 4.2 to include the discriminator network for GAN gives the following equation:

$$\begin{aligned}
& \min_{G_{reg}, G_{cls}} \max_D \mathbb{E}_{x,y \sim \mathbf{Pr}} [\|y - G_{reg}(x) \cdot G_{cls}(x)\|_2^2] + \\
& \quad \mathbb{E}_{x,\hat{y} \sim \mathbf{Pr}} [\hat{y} \cdot \log(G_{cls}(x)) + (1 - \hat{y}) \cdot \log(1 - G_{cls}(x))] + \\
& \quad \mathbb{E}_{x,y \sim \mathbf{Pr}} [\log(D(x, y))] + \mathbb{E}_{x \sim \mathbf{Pr}} [\log(1 - D(x, G_{reg}(x) \cdot G_{cls}(x)))] ,
\end{aligned} \tag{4.5}$$

where D is the discriminator. Unlike the previously discussed discriminator that only looks at the target y or simulated target $G_{reg} \cdot G_{cls}$, here we use a discriminator that also looks at the corresponding input x as reference. This is known as a conditional generative adversarial network (cGAN), as now the discrimination of the true or fake distribution is conditioned on the input x . cGANs have been shown to perform even better than GANs but requires paired x, y data, which is not always readily available Mirza, Osindero (2014). However, in this study, the paired data is provided by spatiotemporal resolution matching of the inputs (GOES-R bands) and the observation data (MRMS). Our setup follows closely to that of Isola et al. (2017) as we consider pixel-wise precipitation estimation from satellite imagery as the image-to-image translation problem from computer vision. The notable differences between our setup and that of Isola et al. (2017) are the generator network structure and objective function. While the objective function of Isola et al. (2017) contains only two parts: L1 on the generator and binary cross-entropy on the discriminator, our final objective function (Eq. 4.5) contains three parts: L2 on the generator, binary cross-entropy on the discriminator, and binary cross-entropy on the output of the classifier. The optimal point for the min-max equation is known from game theory, which is when the discriminator and the generator reach a Nash equilibrium. That's the point when the discriminator is not able to tell the difference between the fake samples and the ground truth data anymore.

The last phase of the methodology considers the infusion of other channels of GOES-16 satellite data and GTOPO30 elevation information as an ancillary data. We first evaluate

selected channels of GOES-16 individually with and without inclusion of elevation data to establish a baseline for how informative each individual channel is for precipitation estimation. We then evaluate combinations of GOES-16 channels to see how well different channels complement each other.

4.4 Results and Discussion

In this section, we evaluate the performance of the proposed algorithm over the verification period for the continental United States. We compare the operational product PERSIANN-CCS, in addition to a baseline model that is trained using conventional and commonly used metric MSE as its objective function. The MRMS data is used as the ground truth data to investigate the performance improvement in both detecting the rain/no-rain pixels and the estimates. Table 4.5 provides the overall statistic performances of the cGAN model compared to PERSIANN-CCS with reference to the MRMS data. Multiple channels are considered stand-alone and as the input to the proposed model including channel 13 with similar wavelength to PERSIANN-CCS to make the comparison fair.

Table 4.5: Statistical evaluation metrics values for different scenarios using single spectral bands

Sc.	Band number/Wavelength (μm)	MSE (mm h^{-1}) ²	COR	BIAS	POD	FAR	CSI	MSE	COR	BIAS	POD	FAR	CSI	
cGAN Model Output														
			Without Elevation						With Elevation					
1	8 – 6.2	1.410	0.270	-0.030	0.356	0.734	0.174	1.096	0.311	-0.017	0.363	0.726	0.180	
2	9 – 6.9	1.452	0.271	-0.044	0.371	0.725	0.182	1.107	0.317	-0.032	0.428	0.736	0.190	
3	10 – 7.3	1.536	0.281	-0.090	0.474	0.755	0.188	1.105	0.313	-0.037	0.450	0.727	0.200	
4	11 – 8.4	1.310	0.271	-0.034	0.507	0.714	0.219	1.053	0.326	-0.047	0.599	0.726	0.229	
5	13 – 10.3	1.351	0.262	-0.041	0.518	0.718	0.220	1.037	0.323	-0.039	0.594	0.731	0.224	
PERSIANN-CCS														
		MSE		COR		BIAS		POD		FAR		CSI		
	10.8 μm	2.174		0.220		-0.046		0.284		0.622		0.193		

The elevation data is also considered as another input to the model along with single bands of ABI GOES-16 to investigate the effect of infusing elevation data as auxiliary information. All evaluation metrics show improved results for the proposed cGAN model over the operational PERSIANN-CCS product during the verification period using band number 13.

Specifically, the application of elevation data combined with single spectral bands indicates further performance improvement. Beside channel 13 as input to the model, utilization of channel 11 ("Cloud Top Phase") as a stand-alone input to the model also shows good performance due to the statistics from evaluation metrics. It could be concluded that channel 11 is also playing an important role as channel 13 in providing useful information for the task of precipitation estimation either utilized as stand-alone or combined with elevation information.

Multiple scenarios are considered as shown in Table 4.6 to investigate the benefit that channels 11 and 13 provide for the model in combination with some other spectral bands including different levels of water vapor. The evaluation metrics values indicate that the utilization of more spectral bands as input to the proposed model (Sc. 9), leads to lower MSE and higher correlation and CSI.

Table 4.6: Statistical evaluation metrics values for different scenarios using multiple spectral bands

Sc.	Band number/Wavelength (μm)	MSE (mm h^{-1}) ²	COR	BIAS	POD	FAR	CSI
cGAN Model Output							
1	8,11 – 6.2, 8.4	1.349	0.353	-0.094	0.635	0.683	0.266
2	9,11 – 6.9, 8.4	1.317	0.345	-0.088	0.627	0.667	0.275
3	10,11 – 7.3, 8.4	1.385	0.343	-0.119	0.668	0.681	0.274
4	8,9,10,11 – 6.2, 6.9, 7.3, 8.4	1.170	0.319	-0.064	0.601	0.658	0.275
5	8,13 – 6.2, 10.3	1.350	0.348	-0.100	0.644	0.689	0.264
6	9,13 – 6.9, 10.3	1.410	0.344	-0.124	0.661	0.678	0.275
7	10,13 – 7.3, 8.4	1.408	0.337	-0.129	0.665	0.676	0.277
8	8,9,10,13 – 6.2, 6.9, 7.3, 10.3	1.258	0.317	-0.077	0.594	0.655	0.274
9	8,9,10,11,12,13,14 – 6.2, 6.9, 7.3, 8.4, 9.6, 10.3, 11.2	1.178	0.359	-0.086	0.706	0.681	0.278
PERSIANN-CCS							
		MSE (mm h^{-1}) ²	COR	BIAS	POD	FAR	CSI
	10.8 μm	2.174	0.220	-0.046	0.284	0.622	0.193

Visualization of predicted precipitation values for the proposed cGAN model and oper-

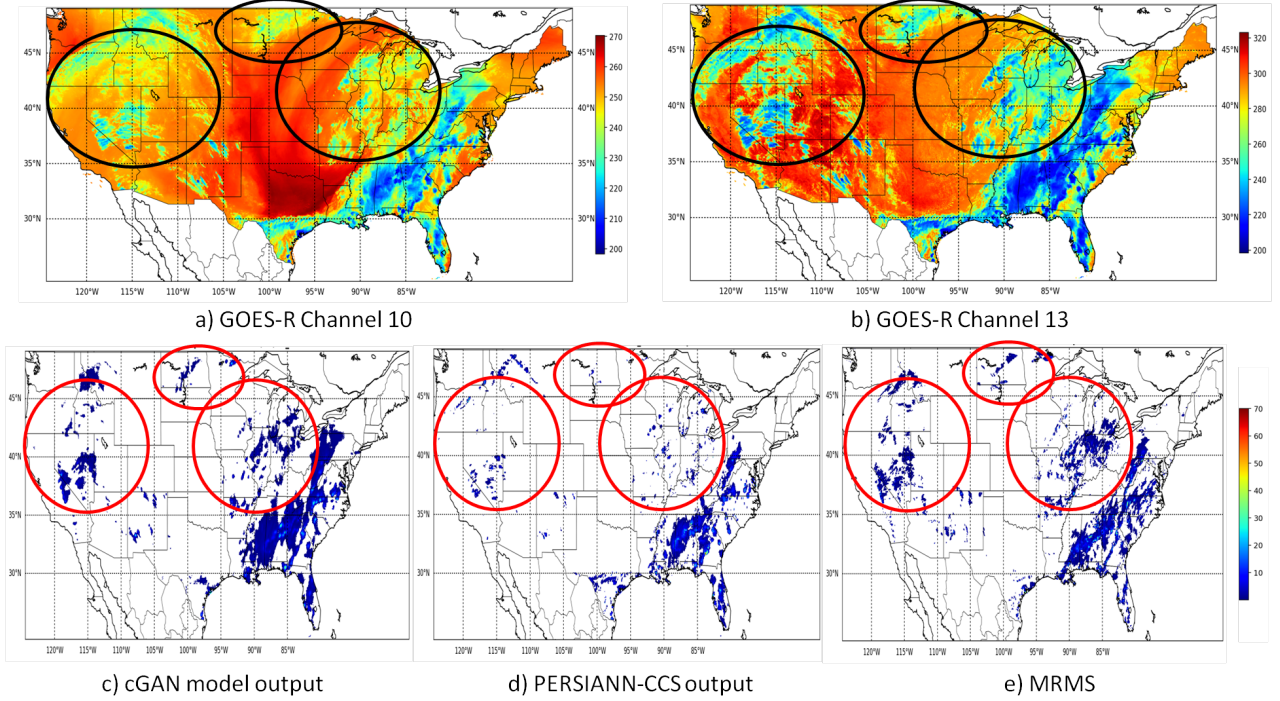


Figure 4.4: a) Channels 10 and b) 13 from ABI GOES-16 imagery, c) cGAN model half hourly output, d) PERSIANN-CCS half hourly precipitation values, and e) The MRMS data for July 31, 2018 at 22:00 UTC over the CONUS. Black circles on GOES-16 satellite imageries are presenting regions with warm clouds and the red circles are the corresponding regions with the rainfall associated with the warm clouds.

ational PERSIANN-CCS product are shown in Figure ?? to emphasize the performance improvement specifically over the regions covered with warm clouds. Capturing clouds with higher temperature associated with rainfall is an important issue that is considered as the main drawback for precipitation retrieval algorithms such as PERSIANN-CCS. This inherent shortcoming is associated with the temperature threshold based segmentation part of the algorithm incapable of fully extracting warm raining clouds (Hayatbini et al., 2019a). Figure 4.4 is showing two sample IR band types and the half-hourly precipitation maps from the proposed model using the inputs listed in the scenario number 9 in Table 4.6 for July 31 at 22:00 - UTC along with the PERSIANN-CCS output and MRMS data for the same time step.

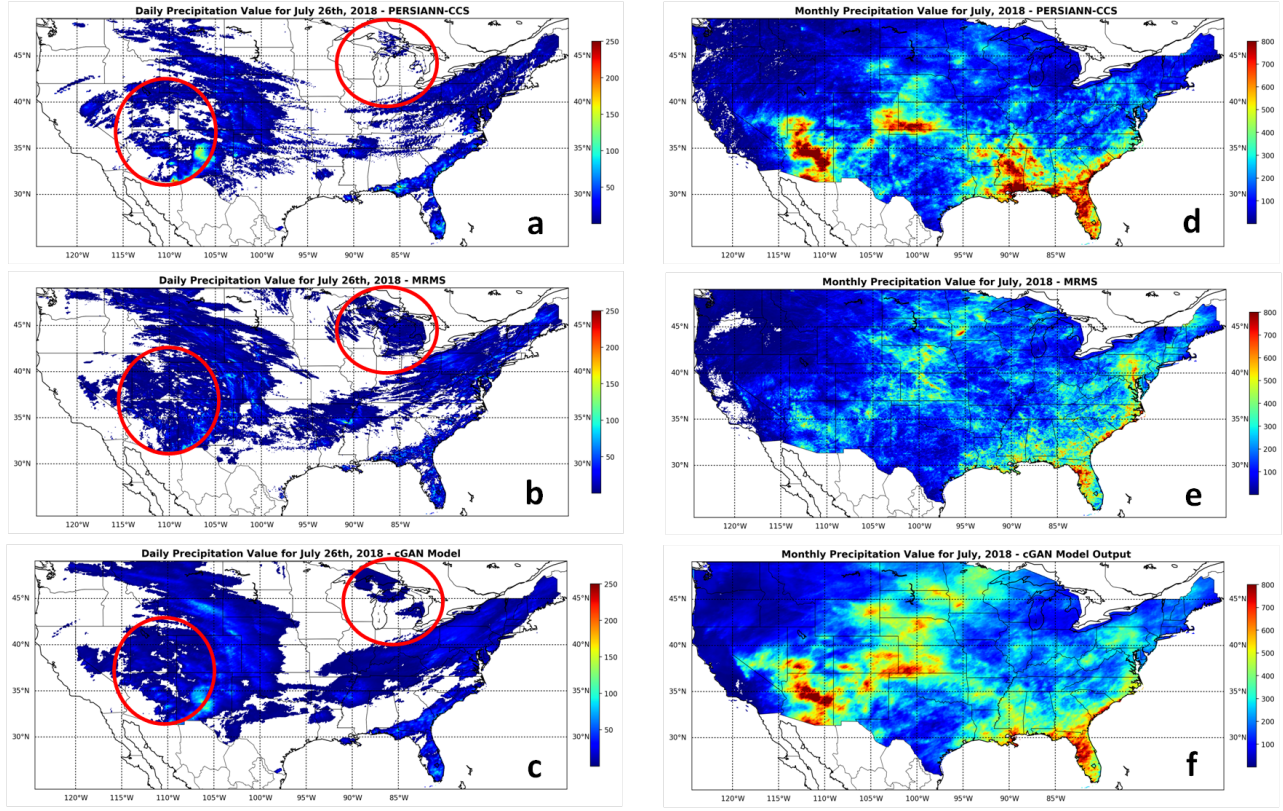


Figure 4.5: Daily (left panel) and monthly (right panel) precipitation values for a&d) PERSIANN-CCS, c&f) cGAN model output compared to the b&e) Reference data - MRMS. Red circles are highlighting regions with most of the differences.

Daily and monthly values for all the models are also provided in Figure 4.5. As shown in the red circled regions for the precipitation values with daily scale in the left panel, the proposed cGAN model output is capturing more of the precipitation as compared to PERSIANN-CCS output. Although both models are showing overestimation compared to MRMS in monthly scale, precipitation values from the proposed model are closer to the ground truth extreme values than PERSIANN-CCS.

Figure 4.6 presents R/NR identification results for the proposed cGAN model and the PERSIANN-CCS models for the 20th of July 2018. It is obvious that only small sections of rainfall are correctly identified by PERSIANN-CCS while cGAN model is able to reduce the missing rainy pixels and shows a significant improvement in delineating the precipitation area, represented by green pixels. More pixels with false detection of rainfall are observed

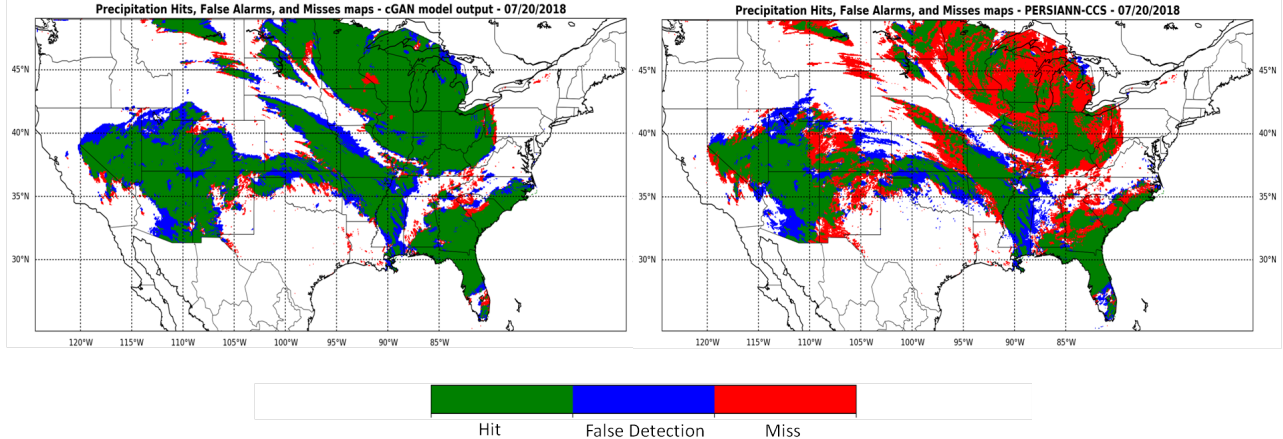


Figure 4.6: Visualization of precipitation identification performance of PERSIANN-CCS vs cGAN model output over the United States for July 20th, 2018.

in cGAN model output than PERSIANN-CCS which are insignificant compared to much higher detection and lower miss of rainy pixels.

Figure 4.7 presents the maps of POD, FAR, and CSI values for the cGAN model compared to PERSIANN-CCS and the baseline model with MSE as the loss function. As explained in the methodology section, the cGAN model’s loss term consists of an additional part other than MSE that has to be optimized as a min-max problem in order to better capture complex precipitation distribution. Figure 4.7 indicates the common verification measurements in Table ?? for regression performance of all three models during the verification period. High measurement values are represented by warm colors and low measurement values are indicated by cold colors. Note that high values are desirable for POD and CSI, while lower values are desirable for FAR. Figure 4.7 shows that the cGAN model outperforms the PERSIANN-CCS almost all over the CONUS and is showing better performance over the baseline model as well. For FAR, higher values observed for cGAN model are negligible considering the significant improvement of POD over the baseline model and PERSIANN-CCS. An ascending order can be observed in the maps of CSI of PERSIANN-CCS, the baseline model, and the cGAN model.

Correlation and MSE values are also visualized to help to better explain the performance

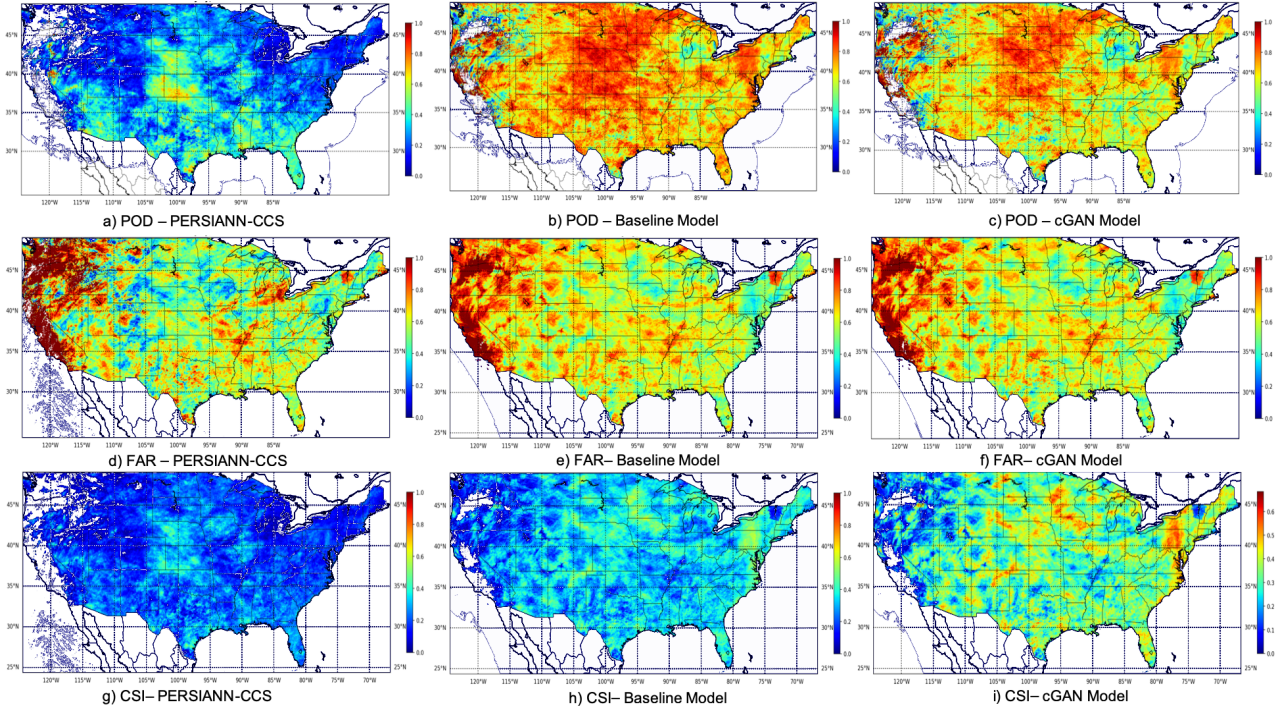


Figure 4.7: POD (top row), FAR (middle row), and CSI (bottom row) of PERSIANN-CCS (left column), the baseline model (middle column), and the cGAN model (right column) over the United States for July 2018.

improvement of the cGAN model over PERSIANN-CCS over the verification period in Figure 4.8.

4.5 Conclusion

This study takes advantage of advanced deep learning techniques, to investigate their capability of effectively and automatically learning the relation between multiple sources of inputs and observation. A two-stage framework using a more complex objective function for training a CNN from multiple channels of latest generation of geostationary satellites is introduced to better capture the complex properties of precipitation. The effectiveness of the proposed model is investigated by comparing it with an operational satellite-based precipitation product (PERSIANN-CCS), and a baseline model with a conventional type of

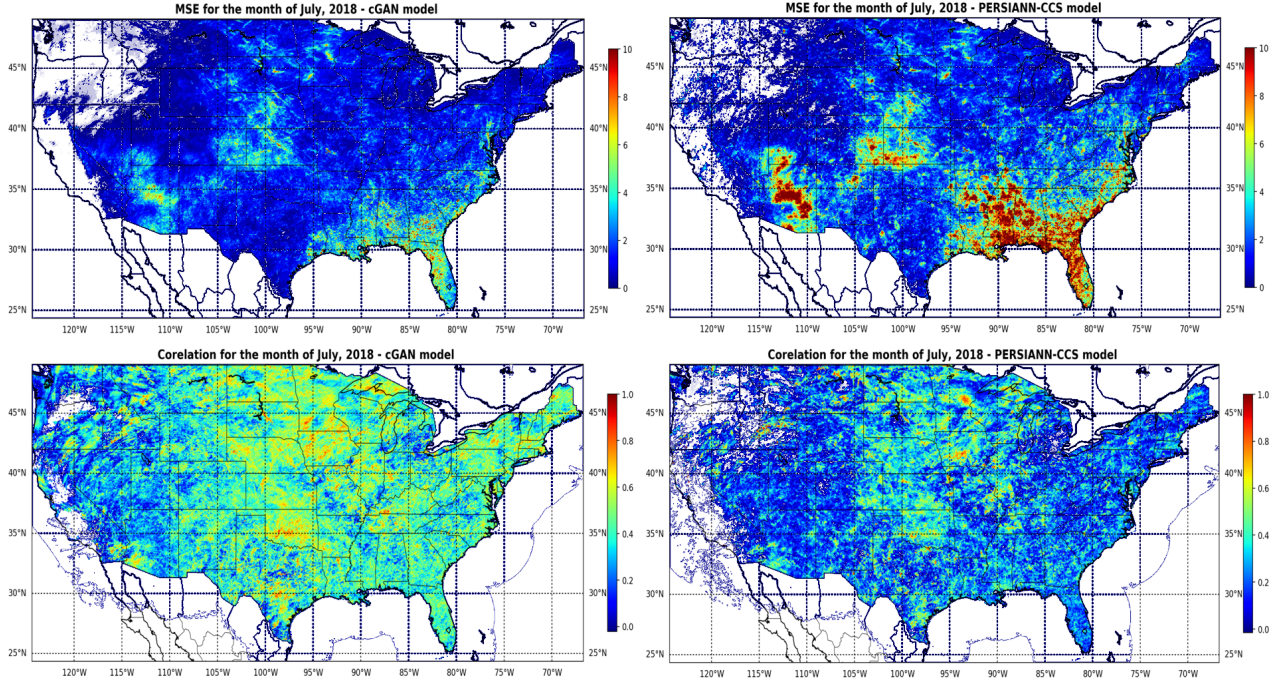


Figure 4.8: The Correlation and MSE values ($mm h^{-1}$)² for the cGAN and PERSIANN-CCS model over the CONUS and during the validation period (month of July 2018).

objective function. The first stage is based on a classification model to delineate precipitation regions and the second stage is a precipitation amount estimation model. The model is calibrated and evaluated over the continental United States.

The evaluation metrics are compared for different scenarios defined to investigate the benefit that each channel provides for the model individually or in combination with other spectral bands. The experimental results demonstrated the general effectiveness of the cGAN two-stage deep learning framework over the PERSIANN-CCS and the baseline model. The proposed model shows the best performance with the application of most of the emissive channels from GOES-16, listed in scenario 9 in Table 4.6 over the verification period which is July 2018 in this study.

The overall performance is improved compared to the baseline model and operational product of PERSIANN-CCS even with the application of IR channel solely as the input of cGAN model to make the comparison fair. The model is capable of capturing the relationship

between the satellite information and the precipitation even at locations covered with warm clouds, which is an important drawback associated with satellite-based precipitation estimation products with global coverage. Moreover, the application of elevation data combined with low number of spectral bands used as input showed performance improvement. We conclude that the model's performance will be improved using the elevation data as an ancillary information to each channel of the satellite and helps the precipitation estimation task to be more accurate and generalized on a larger scale.

Chapter 5

Summary and Conclusion

5.1 Dissertation Summary and conclusion

Precipitation retrieval with high spatiotemporal resolution has always been an important task and an essential element for hydrological and meteorological applications. Improving the accuracy of precipitation estimation from remotely sensed data is more achievable with recent advancements in satellite remote sensing technologies. The availability of large amounts of data also known as big data offers unprecedented opportunities to improve or develop more advanced and reliable precipitation estimation algorithms. One path to reach this goal is to utilize more up-to-dated tools and methodologies for the extraction and exploitation of relevant information linked to precipitation. In this dissertation, state-of-the-art data-driven frameworks are proposed based on deep learning and computer vision tools to extract the most useful features from single or multiple spectral bands of geostationary satellites.

Specifically, a novel gradient-based cloud-image segmentation algorithm is proposed to effectively identify clouds and monitor their evolution towards more accurate quantitative precipitation estimation and forecast. The proposed algorithm integrates morphological im-

age gradient magnitudes to separate cloud systems and patches boundaries from single or multi-spectral imagery. This method improves rain detection and estimation skills with more accurately identifying cloud regions compared to the existing cloud-patch-based segmentation technique implemented in the PERSIANN-CCS as baseline model. The application of this method is extendable to synthetic satellite imageries and hurricanes simulations.

Moreover, a state-of-the-art precipitation estimation framework is developed from multiple sources of information and using advances in deep learning. A Fully Convolutional Network (FCN) is used as a regressor to predict precipitation estimates for rainy pixels that are previously classified using a rain/norain binary mask generated by classification of the pixels. The conditional Generative Adversarial Network (cGAN), and the Mean Squared Error (MSE) loss terms are used to train a network to generate results that better learn the complex distribution of precipitation from the ground truth data. The accuracy of both R/NR classification and real-valued precipitation estimates are evaluated using metrics such as Probability Of Detection (POD), False Alarm Ratio (FAR), Critical Success Index (CSI), Mean Square Error and Correlation. Statistics and visualizations of the evaluation metrics represent improvement in the accuracy of the proposed algorithm compared to the baseline models.

At a high level, the main contributions of this dissertation are as follows:

- Developed and introduced a novel cloud segmentation technique to present cloud types based on their boundaries and regardless of their temperature and height.
- Introduced application of CNNs instead of fully connected networks in extracting useful features from GEO satellite imagery to better capture the spatial and temporal dependencies in satellite-based images.
- Demonstrated the advantage of using a more sophisticated loss function to

better capture the complex distribution of precipitation.

- Proposed a new precipitation retrieval algorithm called PERSIANN-cGAN as a near-real-time high-spatiotemporal rainfall estimation algorithm.
- Evaluated different scenarios of implementing multiple channels of satellite data combinations along with the auxiliary source of information - elevation data - as input to the proposed precipitation retrieval algorithm.

5.2 Future Directions

The algorithms developed in this research have unique capabilities and provide the potential opportunity for future directions and extension. Some potential directions are discussed below.

5.2.1 Additional Data Sources

Data related to precipitation estimation come from a variety of sources, including satellite platforms, radars, and ground-based measurements, each with their strengths and weaknesses. Obviously, the combination of multiple satellite-based observation systems is more potential to provide a more comprehensive and realistic output.

GOE satellite observations, and more particularly Level 2 Cloud and Moisture Imagery Products (CMIP) from the Advanced Baseline Imager (ABI) onboard GOES-16 (NOAA/NASA) are the main source of data used in this research. The CMIP data covers the time range from 2017 to the present with a temporal resolution of 30 seconds to 15 minutes and includes all sixteen channels from the ABI. The algorithms presented in this dissertation are flexible to be extended to other new-generation GEO sensors (Himawari 8/9 AHI, MTG-I/S FCI,

and FY-4 AGRI spectral bands).

Another valuable source of information to better detect the vertical distribution of hydrometeors and the structure of clouds is NASA’s CloudSat Level 2 Cloud Scenario Classification Product. The unique cloud profiling radar (CPR) instrument on NASA’s CloudSat LEO satellite is useful to provide most tropospheric cloud types, along with precipitation identification and the likelihood of mixed-phase conditions. The GPM Microwave Imager (GMI) passive microwave instrument is another candidate to provide microwave radiometric brightness measurements from thirteen channels (Draper et al., 2015).

Numerical weather prediction models are also good supplements for a comprehensive estimation of cloud and precipitation processes. They provide reliable wind profile estimation for solid extrapolation of cloud imagery and demonstrate remarkable accuracy in predicting weather from short to medium range. As shown in chapter 3 of the dissertation, synthetic satellite imagery derived from numerical models may be beneficial for necessary data fusion and algorithm evaluation. Both the operational forecast and the reanalysis product from the Global Forecast System (GFS) from the National Centers for Environmental Prediction (NCEP) are ideal for use in combination with high-resolution atmospheric analysis and prediction.

5.2.2 Model Development

Throughout this dissertation, Convolutional Neural Networks (CNNs), as well as computer vision techniques, are served as the base for the model structures. Computer vision tools and CNNs are great candidates for extracting high-level patterns from images and are suitable for processing satellite imageries. However, there is room for further research on network design (such as hyper-parameters tuning, activation function selection, etc.).

Recurrent Neural Networks (RNNs) are other important tools that can be used to enhance temporal consistency and coordinate differences between different data sources in precipitation estimates. The application of a well-trained RNN model provides prior knowledge of changes in location and surface rainfall rates, which can improve the accuracy of precipitation acquisition. Generative adversarial network and its application in improving DNNs calibration for the task of precipitation estimation are elaborated in chapter 4 of the dissertation. Presented results showed that generative models can further address the complexity existing in the Earth sciences phenomena by matching the distribution of model outputs with the true distribution of the phenomena, thus resulting in a sophisticated understanding of the process and more accurate results. The application of a generative model to combine both CNN and RNN blocks into a unified framework that is trained jointly could be a great direction to maximize the distribution matching process and better simulation of atmospheric dynamics and precipitation distribution.

5.2.3 Operational Application

The current investigation is a preliminary step as a proof of concept for global applications and toward supporting NASA’s GPM mission to develop effective multi-satellite precipitation retrieval algorithms for the fusion of precipitation information from multi-satellite platforms. Future works include organizing a data-driven software package that leverages NASA data sets and can be used in different research areas and other geoscience applications. Further experiments are required for the preparation of the model to serve as an operational product.

Bibliography

- Abdi Ghazem, Samadzadegan Farhad, Reinartz Peter.* Spectral-spatial feature learning for hyperspectral imagery classification using deep stacked sparse autoencoder // Journal of Applied Remote Sensing. 2017. 11, 4. 042604.
- Adams Rolf, Bischof Leanne.* Seeded region growing // IEEE Transactions on pattern analysis and machine intelligence. 1994. 16, 6. 641–647.
- Akbari Asanjan Ata, Yang Tiantian, Hsu Kuolin, Sorooshian Soroosh, Lin Junqiang, Peng Qidong.* Short-Term Precipitation Forecast Based on the PERSIANN System and LSTM Recurrent Neural Networks // Journal of Geophysical Research: Atmospheres. 2018. 123, 22. 12–543.
- Arjovsky Martin, Chintala Soumith, Bottou Léon.* Wasserstein gan // arXiv preprint arXiv:1701.07875. 2017.
- Arkin Phillip A, Meisner Bernard N.* The relationship between large-scale convective rainfall and cold cloud over the western hemisphere during 1982-84 // Monthly Weather Review. 1987. 115, 1. 51–74.
- Behrangi Ali, Hsu Kuo-lin, Imam Bisher, Sorooshian Soroosh, Huffman George J, Kuligowski Robert J.* PERSIANN-MSA: A precipitation estimation method from satellite-based multispectral analysis // Journal of Hydrometeorology. 2009a. 10, 6. 1414–1429.
- Behrangi Ali, Hsu Kuo-lin, Imam Bisher, Sorooshian Soroosh, Kuligowski Robert J.* Evaluating the utility of multispectral information in delineating the areal extent of precipitation // Journal of Hydrometeorology. 2009b. 10, 3. 684–700.
- Bengio Yoshua, Simard Patrice, Frasconi Paolo, others .* Learning long-term dependencies with gradient descent is difficult // IEEE transactions on neural networks. 1994. 5, 2. 157–166.
- Bengio Yoshua, others .* Learning deep architectures for AI // Foundations and trends® in Machine Learning. 2009. 2, 1. 1–127.
- Blaschke Thomas, Hay Geoffrey J, Kelly Maggi, Lang Stefan, Hofmann Peter, Addink Elisabeth, Feitosa Raul Queiroz, Meer Freek Van der, Werff Harald Van der, Van Coillie Frieke, others .* Geographic object-based image analysis—towards a new paradigm // ISPRS journal of photogrammetry and remote sensing. 2014. 87. 180–191.

Chen Chenyi, Seff Ari, Kornhauser Alain, Xiao Jianxiong. Deepdriving: Learning affordance for direct perception in autonomous driving // Proceedings of the IEEE International Conference on Computer Vision. 2015. 2722–2730.

Chen Yanqiao, Jiao Licheng, Li Yangyang, Zhao Jin. Multilayer projective dictionary pair learning and sparse autoencoder for PolSAR image classification // IEEE Transactions on Geoscience and Remote Sensing. 2017. 55, 12. 6683–6694.

Chen Yushi, Lin Zhouhan, Zhao Xing, Wang Gang, Gu Yanfeng. Deep learning-based classification of hyperspectral data // IEEE Journal of Selected topics in applied earth observations and remote sensing. 2014. 7, 6. 2094–2107.

Cho Kyunghyun, Van Merriënboer Bart, Gulcehre Caglar, Bahdanau Dzmitry, Bougares Fethi, Schwenk Holger, Bengio Yoshua. Learning phrase representations using RNN encoder-decoder for statistical machine translation // arXiv preprint arXiv:1406.1078. 2014.

Danielson Jeffrey J, Gesch Dean B. Global multi-resolution terrain elevation data 2010 (GMTED2010). 2011.

Deng Li, Li Jinyu, Huang Jui-Ting, Yao Kaisheng, Yu Dong, Seide Frank, Seltzer Michael, Zweig Geoff, He Xiaodong, Williams Jason, others . Recent advances in deep learning for speech research at Microsoft // 2013 IEEE International Conference on Acoustics, Speech and Signal Processing. 2013. 8604–8608.

Draper David W, Newell David A, Wentz Frank J, Krimchansky Sergey, Skofronick-Jackson Gail M. The global precipitation measurement (GPM) microwave imager (GMI): Instrument overview and early on-orbit performance // IEEE Journal of Selected Topics in Applied Earth Observations and Remote Sensing. 2015. 8, 7. 3452–3462.

Elman Jeffrey L. Finding structure in time // Cognitive science. 1990. 14, 2. 179–211.

Esteva Andre, Kuprel Brett, Novoa Roberto A, Ko Justin, Swetter Susan M, Blau Helen M, Thrun Sebastian. Dermatologist-level classification of skin cancer with deep neural networks // Nature. 2017. 542, 7639. 115.

Gong Maoguo, Yang Hailun, Zhang Puzhao. Feature learning and change feature classification based on deep learning for ternary change detection in SAR images // ISPRS Journal of Photogrammetry and Remote Sensing. 2017. 129. 212–225.

Gonzalez Rafael C, Woods Richard E. Digital image processing Addison. 1992.

Goodfellow Ian. NIPS 2016 tutorial: Generative adversarial networks // arXiv preprint arXiv:1701.00160. 2016.

Goodfellow Ian, Bengio Yoshua, Courville Aaron. Deep Learning. 2016. <http://www.deeplearningbook.org>.

Goodfellow Ian, Pouget-Abadie Jean, Mirza Mehdi, Xu Bing, Warde-Farley David, Ozair Sherjil, Courville Aaron, Bengio Yoshua. Generative adversarial nets // Advances in neural information processing systems. 2014. 2672–2680.

Hagolle Olivier, Huc Mireille, Pascual D Villa, Dedieu Gérard. A multi-temporal method for cloud detection, applied to FORMOSAT-2, VENμS, LANDSAT and SENTINEL-2 images // Remote Sensing of Environment. 2010. 114, 8. 1747–1755.

Hao Siyuan, Wang Wei, Ye Yuanxin, Nie Tingyuan, Bruzzone Lorenzo. Two-stream deep architecture for hyperspectral image classification // IEEE Transactions on Geoscience and Remote Sensing. 2017. 56, 4. 2349–2361.

Hayatbini Negin, Hsu Kuo-lin, Sorooshian Soroosh, Zhang Yunji, Zhang Fuqing. Effective Cloud Detection and Segmentation Using a Gradient-Based Algorithm for Satellite Imagery: Application to Improve PERSIANN-CCS // Journal of Hydrometeorology. 2019a. 20, 5. 901–913.

Hayatbini Negin, Kong Bailey, Hsu Kuo-lin, Nguyen Phu, Sorooshian Soroosh, Stephens Graeme, Fowlkes Charless, Nemani Ramakrishna, Ganguly Sangram. Conditional Generative Adversarial Networks (cGANs) for Near Real-Time Precipitation Estimation from Multispectral GOES-16 Satellite Imageries—PERSIANN-cGAN // Remote Sensing. 2019b. 11, 19. 2193.

He Kaiming, Zhang Xiangyu, Ren Shaoqing, Sun Jian. Deep residual learning for image recognition // Proceedings of the IEEE conference on computer vision and pattern recognition. 2016. 770–778.

Hinton Geoffrey E. Deep belief networks // Scholarpedia. 2009. 4, 5. 5947.

Hochreiter Sepp, Schmidhuber Jürgen. Long short-term memory // Neural computation. 1997. 9, 8. 1735–1780.

Hong Y, Chiang Y-M, Liu Y, Hsu K-L, Sorooshian S. Satellite-based precipitation estimation using watershed segmentation and growing hierarchical self-organizing map // International Journal of Remote Sensing. 2006. 27, 23. 5165–5184.

Hong Y, Hsu K, Sorooshian S. Precipitation estimation from remotely sensed information using ANN-cloud classification system // AGU Fall Meeting Abstracts. 2003.

Hong Yang, Hsu Kuo-Lin, Sorooshian Soroosh, Gao Xiaogang. Precipitation estimation from remotely sensed imagery using an artificial neural network cloud classification system // Journal of Applied Meteorology. 2004. 43, 12. 1834–1853.

Hsu Kou-lin, Gao Xiaogang, Sorooshian Soroosh, Gupta Hoshin V. Precipitation estimation from remotely sensed information using artificial neural networks // Journal of Applied Meteorology. 1997. 36, 9. 1176–1190.

Hsu Kuo-Lin, Behrangi Ali, Imam Bisher, Sorooshian Soroosh. Extreme precipitation estimation using satellite-based PERSIANN-CCS algorithm // Satellite Rainfall Applications for Surface Hydrology. 2010. 49–67.

Huffman George J, Bolvin David T, Braithwaite Dan, Hsu Kuolin, Joyce Robert, Xie Pingping, Yoo Soo-Hyun. NASA global precipitation measurement (GPM) integrated multisatellite retrievals for GPM (IMERG) // Algorithm theoretical basis document, version. 2015. 4. 30.

Huffman George J, Bolvin David T, Nelkin Eric J, Wolff David B, Adler Robert F, Gu Guojun, Hong Yang, Bowman Kenneth P, Stocker Erich F. The TRMM multisatellite precipitation analysis (TMPA): Quasi-global, multiyear, combined-sensor precipitation estimates at fine scales // Journal of hydrometeorology. 2007. 8, 1. 38–55.

Huszár Ferenc. How (not) to train your generative model: Scheduled sampling, likelihood, adversary? // arXiv preprint arXiv:1511.05101. 2015.

Ienco Dino, Gaetano Raffaele, Dupakier Claire, Maurel Pierre. Land cover classification via multitemporal spatial data by deep recurrent neural networks // IEEE Geoscience and Remote Sensing Letters. 2017. 14, 10. 1685–1689.

Isola Phillip, Zhu Jun-Yan, Zhou Tinghui, Efros Alexei A. Image-to-image translation with conditional adversarial networks // Proceedings of the IEEE conference on computer vision and pattern recognition. 2017. 1125–1134.

Jedlovec Gary J, Haines Stephanie L, LaFontaine Frank J. Spatial and temporal varying thresholds for cloud detection in GOES imagery // IEEE Transactions on Geoscience and Remote Sensing. 2008. 46, 6. 1705–1717.

Jordan Michael I. Serial order: A parallel distributed processing approach // Advances in psychology. 121. 1997. 471–495.

Joyce Robert J, Janowiak John E, Arkin Phillip A, Xie Pingping. CMORPH: A method that produces global precipitation estimates from passive microwave and infrared data at high spatial and temporal resolution // Journal of Hydrometeorology. 2004. 5, 3. 487–503.

Karbalaei Negar, Hsu Kuolin, Sorooshian Soroosh, Braithwaite Dan. Bias adjustment of infrared-based rainfall estimation using Passive Microwave satellite rainfall data // Journal of Geophysical Research: Atmospheres. 2017. 122, 7. 3859–3876.

Kidd Chris, Kniveton Dominic R, Todd Martin C, Bellerby Tim J. Satellite rainfall estimation using combined passive microwave and infrared algorithms // Journal of Hydrometeorology. 2003. 4, 6. 1088–1104.

Krizhevsky Alex, Sutskever Ilya, Hinton Geoffrey E. Imagenet classification with deep convolutional neural networks // Advances in neural information processing systems. 2012. 1097–1105.

Lakshmanan Valliappa, Hondl Kurt, Rabin Robert. An efficient, general-purpose technique for identifying storm cells in geospatial images // Journal of Atmospheric and Oceanic Technology. 2009. 26, 3. 523–537.

LeCun Yann, Bengio Yoshua, Hinton Geoffrey. Deep learning // nature. 2015. 521, 7553. 436.

LeCun Yann, Boser Bernhard, Denker John S, Henderson Donnie, Howard Richard E, Hubbard Wayne, Jackel Lawrence D. Backpropagation applied to handwritten zip code recognition // Neural computation. 1989. 1, 4. 541–551.

Levizzani V, Schmetz J, Lutz HJ, Kerkmann J, Alberoni PP, Cervino M. Precipitation estimations from geostationary orbit and prospects for METEOSAT Second Generation // Meteorological Applications. 2001. 8, 1. 23–41.

Lin Daoyu, Fu Kun, Wang Yang, Xu Guangluan, Sun Xian. MARTA GANs: Unsupervised representation learning for remote sensing image classification // IEEE Geoscience and Remote Sensing Letters. 2017. 14, 11. 2092–2096.

Liu Yunjie, Racah Evan, Correa Joaquin, Khosrowshahi Amir, Lavers David, Kunkel Kenneth, Wehner Michael, Collins William, others . Application of deep convolutional neural networks for detecting extreme weather in climate datasets // arXiv preprint arXiv:1605.01156. 2016.

Liu Zhiyong, Zhou Ping, Chen Xiuzhi, Guan Yinghui. A multivariate conditional model for streamflow prediction and spatial precipitation refinement // Journal of Geophysical Research: Atmospheres. 2015. 120, 19.

Lyu Haobo, Lu Hui, Mou Lichao. Learning a transferable change rule from a recurrent neural network for land cover change detection // Remote Sensing. 2016. 8, 6. 506.

Ma Lei, Liu Yu, Zhang Xueliang, Ye Yuanxin, Yin Gaofei, Johnson Brian Alan. Deep learning in remote sensing applications: A meta-analysis and review // ISPRS Journal of Photogrammetry and Remote Sensing. 2019. 152. 166–177.

Mahrooghy Majid, Anantharaj Valentine G, Younan Nicolas H, Aanstoos James, Hsu Kuo-Lin. On an enhanced PERSIANN-CCS algorithm for precipitation estimation // Journal of Atmospheric and Oceanic Technology. 2012. 29, 7. 922–932.

Marzano Frank S, Palmacci Massimo, Cimini Domenico, Giuliani Graziano, Turk F Joseph. Multivariate statistical integration of satellite infrared and microwave radiometric measurements for rainfall retrieval at the geostationary scale // IEEE transactions on Geoscience and remote sensing. 2004. 42, 5. 1018–1032.

Random sets and integral geometry. // . 1975.

Minh Dinh Ho Tong, Ienco Dino, Gaetano Raffaele, Lalande Nathalie, Ndikumana Emile, Osman Faycal, Maurel Pierre. Deep recurrent neural networks for winter vegetation quality mapping via multitemporal SAR Sentinel-1 // IEEE Geoscience and Remote Sensing Letters. 2018. 15, 3. 464–468.

Mirza Mehdi, Osindero Simon. Conditional generative adversarial nets // arXiv preprint arXiv:1411.1784. 2014.

Mou Lichao, Ghamisi Pedram, Zhu Xiao Xiang. Deep recurrent neural networks for hyperspectral image classification // IEEE Transactions on Geoscience and Remote Sensing. 2017. 55, 7. 3639–3655.

Nasrollahi Nasrin, Hsu Kuolin, Sorooshian Soroosh. An artificial neural network model to reduce false alarms in satellite precipitation products using MODIS and CloudSat observations // Journal of Hydrometeorology. 2013. 14, 6. 1872–1883.

Oliehoek Frans A, Savani Rahul, Gallego-Posada Jose, Pol Elise Van der, De Jong Edwin D, Groß Roderich. GANGs: Generative adversarial network games // arXiv preprint arXiv:1712.00679. 2017.

Otkin Jason A, Greenwald Thomas J. Comparison of WRF model-simulated and MODIS-derived cloud data // Monthly Weather Review. 2008. 136, 6. 1957–1970.

Otsu Nobuyuki. A threshold selection method from gray-level histograms // IEEE transactions on systems, man, and cybernetics. 1979. 9, 1. 62–66.

Pahsa Alper. Morphological image processing with fuzzy logic // Journal of Aeronautics and space Technologies. 2006. 2, 3. 27–34.

Pan Baoxiang, Hsu Kuolin, AghaKouchak Amir, Sorooshian Soroosh. Improving Precipitation Estimation Using Convolutional Neural Network // Water Resources Research. 2019. 55, 3. 2301–2321.

Parvati K, Rao Prakasa, Mariya Das M. Image segmentation using gray-scale morphology and marker-controlled watershed transformation // Discrete Dynamics in Nature and Society. 2008. 2008.

Pu Yunchen, Gan Zhe, Henao Ricardo, Yuan Xin, Li Chunyuan, Stevens Andrew, Carin Lawrence. Variational autoencoder for deep learning of images, labels and captions // Advances in neural information processing systems. 2016. 2352–2360.

Rasp Stephan, Pritchard Michael S, Gentine Pierre. Deep learning to represent subgrid processes in climate models // Proceedings of the National Academy of Sciences. 2018. 115, 39. 9684–9689.

Reichstein Markus, Camps-Valls Gustau, Stevens Bjorn, Jung Martin, Denzler Joachim, Carvalhais Nuno, others . Deep learning and process understanding for data-driven Earth system science // Nature. 2019. 566, 7743. 195.

Roerdink Jos BTM. Computer vision and mathematical morphology // Theoretical Foundations of Computer Vision. 1996. 131–148.

Ronneberger Olaf, Fischer Philipp, Brox Thomas. U-net: Convolutional networks for biomedical image segmentation // International Conference on Medical image computing and computer-assisted intervention. 2015. 234–241.

Schmidhuber Jürgen. Deep learning in neural networks: An overview // Neural networks. 2015. 61. 85–117.

Schmit Timothy J, Gunshor Mathew M, Menzel W Paul, Gurka James J, Li Jun, Bachmeier A Scott. Introducing the next-generation Advanced Baseline Imager on GOES-R // Bulletin of the American Meteorological Society. 2005. 86, 8. 1079–1096.

Schmit Timothy J, Menzel W Paul, Gurka J, Gunshor M. The ABI on GOES-R // Proc. 3rd Annu. Symp. Future Nat. Oper. Environ. Satellite Syst. 2010.

Serra Jean. Image analysis and mathematical morphology. 1983.

Shen Dinggang, Wu Guorong, Suk Heung-II. Deep learning in medical image analysis // Annual review of biomedical engineering. 2017. 19. 221–248.

Silver David, Huang Aja, Maddison Chris J, Guez Arthur, Sifre Laurent, Van Den Driessche George, Schrittwieser Julian, Antonoglou Ioannis, Panneershelvam Veda, Lanctot Marc, others . Mastering the game of Go with deep neural networks and tree search // nature. 2016. 529, 7587. 484.

Simonyan Karen, Zisserman Andrew. Very deep convolutional networks for large-scale image recognition // arXiv preprint arXiv:1409.1556. 2014.

Skamarock WC, Klemp JB, Dudhia J, Gill DO, Barker DM, Duda MG, Huang XY, Wang W, Powers JG. A description of the advanced research WRF Version 3, NCAR technical note, Mesoscale and Microscale Meteorology Division // National Center for Atmospheric Research, Boulder, Colorado, USA. 2008.

Soille Pierre, Pesaresi Martino. Advances in mathematical morphology applied to geoscience and remote sensing // IEEE Transactions on Geoscience and Remote Sensing. 2002. 40, 9. 2042–2055.

Sorooshian Soroosh, AghaKouchak Amir, Arkin Phillip, Eylander John, Foufoula-Georgiou Efi, Harmon Russell, Hendrickx Jan MH, Imam Bisher, Kuligowski Robert, Skahill Brian, others . Advanced concepts on remote sensing of precipitation at multiple scales // Bulletin of the American Meteorological Society. 2011. 92, 10. 1353–1357.

Sorooshian Soroosh, Hsu Kuo-Lin, Gao Xiaogang, Gupta Hoshin V, Imam Bisher, Braithwaite Dan. Evaluation of PERSIANN system satellite-based estimates of tropical rainfall // Bulletin of the American Meteorological Society. 2000. 81, 9. 2035–2046.

Sun Lin, Wei Jing, Wang Jian, Mi Xuetong, Guo Yamin, Lv Yang, Yang Yikun, Gan Ping, Zhou Xueying, Jia Chen, others . A universal dynamic threshold cloud detection algorithm (UDTCDA) supported by a prior surface reflectance database // Journal of Geophysical Research: Atmospheres. 2016. 121, 12. 7172–7196.

Szegedy Christian, Ioffe Sergey, Vanhoucke Vincent, Alemi Alexander A. Inception-v4, inception-resnet and the impact of residual connections on learning // Thirty-First AAAI Conference on Artificial Intelligence. 2017.

Tao Yumeng, Gao Xiaogang, Hsu Kuolin, Sorooshian Soroosh, Ihler Alexander. A deep neural network modeling framework to reduce bias in satellite precipitation products // Journal of Hydrometeorology. 2016. 17, 3. 931–945.

Tao Yumeng, Gao Xiaogang, Ihler Alexander, Sorooshian Soroosh, Hsu Kuolin. Precipitation identification with bispectral satellite information using deep learning approaches // Journal of Hydrometeorology. 2017. 18, 5. 1271–1283.

Tao Yumeng, Hsu Kuolin, Ihler Alexander, Gao Xiaogang, Sorooshian Soroosh. A two-stage deep neural network framework for precipitation estimation from Bispectral satellite information // Journal of Hydrometeorology. 2018. 19, 2. 393–408.

Vandal Thomas, Kodra Evan, Ganguly Auroop R. Intercomparison of machine learning methods for statistical downscaling: The case of daily and extreme precipitation // Theoretical and Applied Climatology. 2017. 1–14.

Vincent Luc, Soille Pierre. Watersheds in digital spaces: an efficient algorithm based on immersion simulations // IEEE Transactions on Pattern Analysis & Machine Intelligence. 1991. 6. 583–598.

Vincent Pascal, Larochelle Hugo, Bengio Yoshua, Manzagol Pierre-Antoine. Extracting and composing robust features with denoising autoencoders // Proceedings of the 25th international conference on Machine learning. 2008. 1096–1103.

Wang Cong, Zhang Lei, Wei Wei, Zhang Yanning. When low rank representation based hyperspectral imagery classification meets segmented stacked denoising auto-encoder based spatial-spectral feature // Remote Sensing. 2018. 10, 2. 284.

Wang Demin. A multiscale gradient algorithm for image segmentation using watersheds // Pattern recognition. 1997. 30, 12. 2043–2052.

Xingjian SHI, Chen Zhourong, Wang Hao, Yeung Dit-Yan, Wong Wai-Kin, Woo Wang-chun. Convolutional LSTM network: A machine learning approach for precipitation nowcasting // Advances in neural information processing systems. 2015. 802–810.

Xu Kuan-Man, Wong Takmeng, Wielicki Bruce A, Parker Lindsay, Eitzen Zachary A. Statistical analyses of satellite cloud object data from CERES. Part I: Methodology and preliminary results of the 1998 El Niño/2000 La Niña // Journal of climate. 2005. 18, 13. 2497–2514.

Zahraei Ali, Hsu Kuo-lin, Sorooshian Soroosh, Gourley Jonathan J, Hong Yang, Behrang Ali. Short-term quantitative precipitation forecasting using an object-based approach // Journal of hydrology. 2013. 483. 1–15.

Zhan Ying, Wu Kang, Liu Wei, Qin Jin, Yang Zhaoying, Medjadba Yasmine, Wang Guian, Yu Xianchuan. Semi-supervised classification of hyperspectral data based on generative adversarial networks and neighborhood majority voting // IGARSS 2018-2018 IEEE International Geoscience and Remote Sensing Symposium. 2018. 5756–5759.

Zhang Fuqing, Minamide Masashi, Nystrom Robert G, Chen Xingchao, Lin Shian-Jian, Harris Lucas M. Improving Harvey Forecasts with Next-Generation Weather Satellites: Advanced Hurricane Analysis and Prediction with Assimilation of GOES-R All-Sky Radiances // Bulletin of the American Meteorological Society. 2019. 100, 7. 1217–1222.

Zhang Fuqing, Weng Yonghui, Gamache John F, Marks Frank D. Performance of convection-permitting hurricane initialization and prediction during 2008–2010 with ensemble data assimilation of inner-core airborne Doppler radar observations // Geophysical Research Letters. 2011. 38, 15.

Zhang Fuqing, Weng Yonghui, Sippel Jason A, Meng Zhiyong, Bishop Craig H. Cloud-resolving hurricane initialization and prediction through assimilation of Doppler radar observations with an ensemble Kalman filter // Monthly Weather Review. 2009. 137, 7. 2105–2125.

Zhang Liangpei, Zhang Lefei, Du Bo. Deep learning for remote sensing data: A technical tutorial on the state of the art // IEEE Geoscience and Remote Sensing Magazine. 2016. 4, 2. 22–40.

Zhang Xiaodong, Jia Fucang, Luo Suhuai, Liu Guiying, Hu Qingmao. A marker-based watershed method for X-ray image segmentation // Computer methods and programs in biomedicine. 2014. 113, 3. 894–903.

Zhang Yunji, Zhang Fuqing, Stensrud David J. Assimilating All-Sky Infrared Radiances from GOES-16 ABI using an Ensemble Kalman Filter for Convection-Allowing Severe Thunderstorms Prediction // Monthly Weather Review. 2018. 2018.

Zhu Xiao Xiang, Tuia Devis, Mou Lichao, Xia Gui-Song, Zhang Liangpei, Xu Feng, Fraundorfer Friedrich. Deep learning in remote sensing: A comprehensive review and list of resources // IEEE Geoscience and Remote Sensing Magazine. 2017. 5, 4. 8–36.

Zhu Zhe, Wang Shixiong, Woodcock Curtis E. Improvement and expansion of the Fmask algorithm: Cloud, cloud shadow, and snow detection for Landsats 4–7, 8, and Sentinel 2 images // Remote Sensing of Environment. 2015. 159. 269–277.